A possible new UHP unit in the Western Alps as revealed by ancient Roman quern-stones from Costigliole Saluzzo, Italy

Cover page

Title: A new UHP unit in the Western Alps possibly revealed by ancient Roman quern-stones from Costigliole Saluzzo, Italy

Running title: Ancient quern-stones might reveal a new UHP unit in the Alps

Detailed plan of the article (i.e. hierarchy of headings and subheadings)

Corresponding author:
Simona Ferrando
simona.ferrando@unito.it
Tel. +39/0116705106
Fax: +39/0116705128

Title page

A new UHP unit in the Western Alps possibly revealed by ancient Roman quern-stones from Costigliole Saluzzo, Italy

Chiara Groppo[1,2], Simona Ferrando[1*], Daniele Castelli[1], Diego Elia[3], Valeria Meirano[3], Luca Facchinetti[3]

[1]Department of Earth Sciences, Via Valperga Caluso 35, I-10128 Torino, Italy
[2]IGG-CNR, Via Valperga Caluso 35, I-10128 Torino, Italy
[3]Department of Historical Studies, Via S. Ottavio 20, I-10124 Torino, Italy
*simona.ferrando@unito.it

Abstract

Peculiar coesite + chloritoid + garnet ± glaucophane talcschists have been used to make at least six quern-stones, unearthed in the ruins of a *villa rustica* belonging to the Roman imperial period and located at Costigliole Saluzzo, Western Alps. The site of the *villa rustica* and the presence of coesite relics suggest a possible provenience of these rocks from the ultra-high pressure (UHP) Brossasco-Isasca Unit (BIU) of the southern Dora-Maira Massif. However, similar talcschists have never been reported from this Unit.

Two samples of coesite-bearing, chloritoid + garnet ± glaucophane –talcschist collected from two different specimens of quern-stones, have been petrologically investigated with the aim of constraining their peak P-T conditions. The stability field of the coesite + garnet + talc + chloritoid + glaucophane assemblage has been constrained using isochemical phase diagrams modelled in the MnNCFMASHO system; prograde P-T conditions have been additionally constrained using the yittrium-in-garnet (YAG) geothermometer. Thermodynamic modelling tightly constrains peak P-T conditions at 480-510°C, 27-31 kbar.

The unusual Mg-rich composition of the talcschists suggest that they originated by Mg-metasomatism of either a granodioritic protolith or a Fe-rich metapelitic protolith. A mechanism similar to that constrained for the well-known pyrope-bearing whiteschists of the UHP BIU, i.e. influx of antigorite-derived fluids along shear zones during subduction, can be therefore envisaged.

Although the field occurrence of these coesite + chloritoid + garnet ± glaucophane talcschists is still unknown, the obtained results clearly show that these rocks cannot belong to the UHP BIU, whose peak P-T conditions are at significantly higher T and P (730°C, 40-43 kbar). Therefore, this finding opens the challenging hypothesis of the existence of a further, still unmapped, UHP Unit in the Southern Dora-Maira Massif that also experienced UHP metamorphism and fluid influx from underlying serpentinites during subduction. A detailed mapping and petrologic investigation of the tectono-metamorphic units adjacent to the BIU is required, in order to further constrain the location and the dimension of this new UHP unit in the framework of the southern Dora-Maira Massif.

Key-words: coesite + chloritoid + garnet + glaucophane talcschist; UHP metamorphism; Mg-metasomatism; southern Dora-Maira Massif; thermodynamic modeling; micro-Raman spectroscopy

1. Introduction

The ruins of a wide *villa rustica* belonging to the Roman imperial period were unearthed at the southern periphery of the modern village of Costigliole Saluzzo (Fig. 1) and are still under excavation (Elia & Meirano 2012; Elia *et al*., 2013). In its major phase, the main building reached an extent of around 5000 square metres. The evidence recovered supports the identification of two different sections in the *villa*, the *pars urbana*, with a residential function, and the *pars rustica*, destined to stocking agricultural products and to housing the productive units. Many fragments of quern-stones, pertaining to at least 6 specimens, were retrieved in the building, mainly from a wide room which acted as a kitchen and a butlery as well (Fig. 1b). The majority of the artefacts were in use when the villa was destroyed by a fire at the end of the III c. AD. The hand-mills, up to 34-39 cm in diameter (Fig. 2a,b), belong to two different types: a simpler and more common one, and a second type provided with a particular mechanism in order to obtain different qualities of refined cereals (Fig. 2c). They were carved from at least two different lithologies: (i) a coesite-bearing (micro-Raman identification), chloritoid + garnet ± glaucophane –talcschist (Fig. 2d-f), and (ii) a phengite + garnet + chloritoid ± glaucophane schist, with glaucophane pseudomorphically replaced by fine-grained aggregates of white mica + biotite + albite.

The location of the ancient quarry is still unknown. Costigliole Saluzzo is located at the mouth of Varaita Valley, some 5 km east of the ultra-high pressure (UHP) Brossasco-Isasca Unit (BIU), tectonically sandwiched between the high-pressure (HP) San Chiaffredo and Rocca Solei Units of the southern Dora-Maira Massif (Compagnoni *et al*., 2012; Castelli *et al*., 2014, with refs.) (Fig. 1a). The site of the *villa rustica*, then, clearly points to a provenience of these rocks from the southern Dora-Maira Massif. The presence of coesite relics seems to constrain the area of provenience to the UHP BIU. However, talcschists with a similar mineral assemblage have never been reported from this Unit. Therefore, this finding opens two challenging hypotheses: (i) the occurrence of still unrecognized, peculiar “whiteschist” within the BIU; (ii) the existence of a second, still unmapped, UHP unit in the southern Dora-Maira Massif.

In order to solve this conundrum, two samples of coesite-bearing, chloritoid + garnet ± glaucophane –talcschist collected from two different specimens of quern-stones, have been petrologically investigated with the aim of constraining their peak P-T conditions. The stability field of the coesite + garnet + talc + chloritoid + glaucophane assemblage has been constrained using isochemical phase diagrams modelled in the MnNCFMASHO system. Prograde P-T conditions have been additionally constrained using the yittrium-in-garnet (YAG) geothermometer. The genesis of these talcschists is discussed, considering two different possibilities: (i) derivation from a Mg-rich protolith metamorphosed in a closed system, or (ii) metasomatic product of a mafic or felsic (either granodiorite or metapelite) protolith.

The obtained results clearly suggest the existence of an UHP unit, whose peak P-T conditions lies inside the coesite stability field but at significantly lower temperature than those estimated for the BIU. A detailed mapping and petrologic investigation of the tectono-metamorphic units adjacent to the BIU is required, in order to further constrain the location and the dimension of this new UHP unit in the framework of the southern Dora-Maira Massif.

2. Methods

2.1 Micro-X-ray fluorescence (µ-XRF) maps

The micro-XRF maps of the whole thin sections (Fig. 3) were acquired using a µ-XRF Eagle III-XPL spectrometer equipped with an EDS Si(Li) detector and with an Edax Vision32 microanalytical system

(Department of Earth Sciences, University of Torino, Italy). The operating conditions were as follows: 100 ms counting time, 40 kV accelerating voltage and a probe current of 900 µA. A spatial resolution of about 65 µm in both x and y directions was used. Quantitative modal percentages of each mineral were obtained by processing the µ-XRF maps with the software program ''Petromod'' (Cossio *et al*. 2002).

2.2 Micro-Raman spectroscopy

Micro-Raman spectra and map were acquired using the integrated micro/macro-Raman LABRAM HRVIS (Horiba Jobin Yvon Instruments) of the Interdepartmental Center "G. Scansetti" (Department of Earth Sciences, University of Torino, Italy), equipped with a computer-controlled, automated X–Y mapping stage. Excitation lines at 532 nm (solid-state Nd laser and 80 mW of emission power) were used, with Edge filter and a grating of 600 grooves/mm. Calibration was performed using the 520.6 cm^{-1} Si band. Each spectrum was collected by three accumulations of 5 s and with a laser spot of 4 µm. The map of 140 µm x 45 µm, with steps of 1 µm and a laser spot of 4 µm, was acquired on the sample surface by one accumulations of 1 s each step.

2.3 Mineral chemistry

Minerals were analysed with a Cambridge Stereoscan 360 SEM equipped with an EDS Energy 200 and a Pentafet detector (Oxford Instruments) at the Department of Earth Sciences, University of Torino. The operating conditions were as follows: 50 s counting time and 15 kV accelerating voltage. SEM–EDS quantitative data (spot size = 2 µm) were acquired and processed using the Microanalysis Suite Issue 12, INCA Suite version 4.01; natural mineral standards were used to calibrate the raw data; the $\rho\phi Z$ correction (Pouchou & Pichoir, 1988) was applied. Absolute error is 1 σ for all calculated oxides.

A JEOL 8200 Superprobe (WDS) was used at the Department of Earth Sciences, University of Milano (Italy). Acceleration voltage was set to 15 kV, beam current was 15 nA and natural minerals were used as standards. A $\rho\phi Z$ routine was used for matrix correction.

Mineral chemical data of representative minerals are reported in Fig.5, 6 and in Tables 1-2.

2.4 YAG (yittrium-in-garnet) thermometry

Temperature conditions for the growth of garnet core have been constrained by applying the yittrium-in-garnet thermometry (YAG) of Pyle & Spear (2000). This empirical geothermometer correlates the yittirum content in garnet with its temperature of formation, and is particularly suitable for xenotime-bearing metapelites that experienced metamorphic temperature in the range 450-550 °C; errors estimated in this temperature interval are, in fact, of few degrees.

2.5 Phase diagrams computation

Isochemical phase diagrams were calculated in the MnNCFMASHO system using Perple_X (version 6.7.2, Connolly 1990, 2009) and the thermodynamic dataset and equation of state for H_2O–CO_2 fluid of Holland & Powell (2011). The following solid solution models were used: garnet (White *et al*., 2005), talc (ideal), chloritoid (Smye *et al*., 2000), carpholite (Smye *et al*., 2000), staurolite (ideal), chlorite (Holland *et al*., 1998), Na-amphibole (Dale *et al*., 2000), plagioclase (Newton *et al*., 1980), omphacite (Diener & Powell, 2011) and epidote (Holland & Powell, 1998). Kyanite, quartz/coesite, lawsonite, paragonite, magnetite and hematite were considered as pure end-members.

The bulk rock compositions of the studied samples have been calculated by combining the mineral proportions obtained from the modal estimate of micro-XRF maps (Fig. 3) with mineral

chemistry acquired at SEM–EDS and WDS, and are reported in Table 3: these whole rock compositions have been used to model the growth of garnet core, in equilibrium with chloritoid and glaucophane cores. The possible effects of chemical fractionation of the bulk composition due to the growth of the strongly zoned garnet porphyroblasts have been also considered. The bulk compositions effectively in equilibrium during the growth of garnet rim have been therefore calculated by subtracting the garnet core and mantle compositions to the whole rock compositions (Table 3).

3. Petrography, mineral chemistry and Raman spectroscopy

The coesite-bearing chloritoid + garnet + glaucophane -talcschists (samples US900 and US773) consist of quartz/coesite, talc, garnet, chloritoid, glaucophane, late Mg-chlorite (Fig.3, 4), abundant accessory rutile, apatite and pyrite and minor xenotime (both in the matrix and in garnet). Mineral assemblages and compositions are similar in both the samples, but mineral modes are quite different. Sample US900 is quartz/coesite-, talc- and glaucophane -richer (vol%: Qz 38, Tlc 30, Cld 14, Gln 9, Grt 8; mineral abbreviation after Whitney & Evans, 2010) than sample US773. Sample US773 is chloritoid-richer than sample US900 and contains abundant Mg-chlorite, derived from chloritoid retrogression (vol%: Qz 21, Tlc 22, Cld 23, Mg-Chl 23, Gln 3, Grt 8) (Fig. 3 and Table 3). Although rich in talc, these rocks do not show a pervasive schistosity, due to the presence of garnet, chloritoid and glaucophane porphyroblasts up to few millimetre in size, which partially obliterate the oriented structure.

Chloritoid occurs as bluish-green, slightly zoned, porphyroblasts, with a darker core and a lighter rim (Fig. 4f). It is locally pervasively replaced by a greenish Mg-chlorite, especially in sample US773. Its X_{Mg} ranges from 0.29 in the core to 0.38 in the rim, whereas XFe^{+3} is slightly higher in the core than in the rim (core: X_{Fe+3} = 0.05-0.08; rim: X_{Fe+3} = 0.04-0.07) (Fig. 5d and Table 2) [X_{Mg}=Mg/(Mg+Fe); XFe^{+3}=Fe^{+3}/(Fe^{+3}+Al)].

Garnet porphyroblasts are idioblastic and strongly zoned (Fig. 4a-d), with a reddish core (X_{Fe}=0.73-0.79, X_{Mg}=0.07-0.09, X_{Mn}=0.05-0.12, X_{Ca}=0.08-0.10), a pink mantle (X_{Fe}=0.79-0.83, X_{Mg}=0.09-0.12, X_{Mn}=0.01-0.04, X_{Ca}=0.05-0.08) and a colourless rim (X_{Fe}=0.76-0.79, X_{Mg}=0.13-0.29, X_{Mn}=0.00-0.01, X_{Ca}=0.04-0.06) (Table 1, Fig. 6a and Fig. S1, freely available online as Supplementary Material linked to this article on the GSW website of the journal, http://eurjmin.geoscienceworld.org/). The bell-shaped profile of Mn suggests a prograde garnet growth (Fig. 6b). Similarly to Mn, Y, Cr and Na contents also show a bell-shaped profile (Fig. 6b). Maximum Y, Na and Cr contents in garnet core are 2000, 730, and 480 ppm, respectively, and decreases to almost zero in garnet rim. P has an opposite trend: it is almost absent in garnet core and increases toward the rim, up to 220 ppm.

The garnet core and mantle includes chloritoid (X_{Mg}=0.21-0.24; X_{Fe+3}=0.07-0.10) (Fig. 6d and Fig. S1), very rare and fine-grained phengite (Si = 3.30 a.p.f.u. on the basis of 11 oxygens) locally associated to chloritoid, and rare ilmenite (especially in the garnet core). The garnet mantle and rim preserves relict coesite, partially inverted to quartz (Fig. 4c,d and Fig. S1). The garnet rim locally includes talc, whereas fine-grained rutile is ubiquitous as inclusion in garnet.

Coesite inclusions preserved in garnet mantle are quite big (up to 200 μm) and poorly retrogressed to quartz (Fig. 7a), compared to coesite included in garnet rim, that is mostly replaced by quartz with a palisade structure (Fig. 7b) or by polycrystalline quartz (Fig. 7a). Garnet surrounding the coesite inclusions shows the typical radial fractures due to the volume increase related to the coesite-quartz inversion (Fig. 4c,d; Fig. 7b). The presence of coesite is confirmed by micro-Raman analyses on exposed inclusions (Fig. 7c), which show the typical coesite vibrations (Frezzotti *et al.*,

2011). The upshift of most, but not all, of coesite peaks (e.g., the main peak at 523 cm^{-1} instead of 521 cm^{-1}) indicates that a residual pressure is still preserved in the inclusions (e.g., Korsakov *et al.*, 2007; Khon, 2014). The best preserved, although exposed, single coesite inclusion has been selected for Raman mapping (Fig. 7d). Also this coesite preserves a residual pressure (main peak at 524 cm^{-1}). Quartz is optically detectable only in two cracks crosscutting the inclusion (Fig. 7d). Raman map (Fig. 7e) confirms the presence of quartz along the cracks, but also reveals the distribution of optically undetectable quartz (i) as thin shell of 1-5 μm in thickness that completely surrounds the coesite inclusion, and (ii) as thin veinlets (<5 μm in thickness) cutting the coesite. The main peak of quartz at 470 cm^{-1} instead of 464 cm^{-1} indicates an high residual pressure due to the coesite-to-quartz transition (e.g., Korsakov *et al.*, 2009). These data confirm that the initial stage of inversion from coesite to quartz subgrains occurs at grain boundaries between coesite and hosting garnet, and along crosscutting cracks (e.g., Korsakov *et al.*, 2007).

A slightly-zoned, bluish to colourless glaucophane (abundant in sample US900: Fig. 3, 4a) is in equilibrium with both chloritoid (Fig. 4e) and garnet rims and with talc. Its X_{Mg} and X_{Fe+3} are slightly variable from core to rim (core: X_{Mg} = 0.70-0.74, X_{Fe+3} = 0.20-0.33; rim: X_{Mg} = 0.72-0.76, X_{Fe+3} = 0.14-0.23) (Fig. 5a-c and Table 2). In the more retrograded sample US773, glaucophane is locally surrounded by a thin and discontinuous rim of Na-Ca amphibole (winchite).

Talc has a X_{Mg}=0.85-0.88 (Table 2). Mg-chlorite is a late phase, developed at the expenses of chloritoid in sample US7773 (Fig. 4b, f). Its composition is quite homogeneous, with a X_{Mg} = 0.60-0.71 (Table 2). Very rare epidote has also been observed in sample US773, and seems in equilibrium with Mg-chlorite.

4. Phase equilibria and P-T evolution

4.1 Stability field of the chloritoid + glaucophane + garnet ± talc assemblage: previous studies

Chloritoid + glaucophane ± garnet and chloritoid + garnet + talc ± glaucophane assemblages are typical of blueschists and low-T eclogites in high-pressure terranes around the world. The coexistence of chloritoid + glaucophane ± garnet is reported in metapelitic rocks from the Variscan Ile de Groix (Kienast & Triboulet, 1972; Bosse *et al*., 2002), Vendée (Guiraud *et al*., 1987) and Iberian Massif (Lopez-Carmona *et al*., 2010), the Gran Paradiso Massif of the western Alps (Chopin, 1981), the Peloponnese in Greece (Katagas, 1980; Theye & Seidel, 1991), Turkey (Okay, 2002), Oman (El-Shazly & Liou, 1991; Warren & Waters, 2006), New Caledonia (Ghent *et al*., 1987), Sulawesi in Indonesia (Miyazaki *et al*., 1996), and the Chinese Tianshan (Wei *et al*., 2009) and Qilian orogens (Wei & Song, 2008).

Talc + chloritoid ± garnet ± glaucophane assemblages, similar to that observed in the studied samples, are more rarely reported. They were described from the Gran Paradiso and Monte Rosa Massifs of the western Alps (silvery micaschist: Compagnoni & Lombardo, 1974; Chopin, 1981; Chopin & Moniè, 1984; Dal Piaz & Lombardo, 1986; Goffè & Chopin, 1986; Meffan-Main *et al*., 2004; Gabudianu Radulescu *et al*., 2009), the Chinese Qilian orogen (Wei & Song, 2008) and the Tianshan of Kazakhstan and Kyrgyzstan (Meyer *et al*., 2014; Klemd *et al*., 2015; Orozbaev *et al*., 2015). This last occurrence is worth of note, because of the presence of coesite relicts included in garnet.

Thermodynamic calculations in the model system NFMASH, NKFMASH and NCKFMASH (e.g. Guiraud *et al*., 1990; Proyer, 2003; Wei & Powell, 2004, 2006) suggested that the chloritoid + glaucophane ± garnet assemblage is a high-pressure indicator in metapelites, being stable at pressures higher than 18-19 kbar (except for Fe-rich compositions, where this assemblage is stable at pressures as lower as 7-8 kbar: Wei & Song, 2008). The maximum stability field of the chloritoid +

glaucophane ± garnet assemblage is constrained at P = 19-35 kbar and T = 420-610 °C. In the quartz stability field, this assemblage provides tight temperature constraints, being limited by the appearance of the carpholite + jadeite assemblage at temperatures lower than ca. 420-430 °C and by the appearance of garnet + kyanite + talc at temperature higher than ca. 600-610 °C. At pressures above the quartz-coesite transition, the high-T boundary of this assemblage is still located at about 600 °C, whereas the low-T boundary is more P-dependent resulting in a field assemblage progressively narrower toward high-P (Proyer, 2003; Wei & Powell, 2004, 2006). Furthermore, chloritoid + glaucophane ± garnet assemblage is easily preserved during exhumation because it requires external hydration in order to breakdown to lower pressures (Proyer, 2003).

The addition of talc results in a further limitation of the talc + chloritoid + glaucophane + garnet stability field, limited at lower temperatures by the appearance of carpholite + chlorite/garnet at about 530-550°C. This assemblage is predicted to be stable also at ultra-high pressure conditions, in the narrow temperature range of about 550-600°C for P < 35 kbar (Proyer, 2003; Wei & Powell, 2004, 2006; Franz *et al*., 2013).

4.2 Thermodynamic modelling of the chloritoid + glaucophane + garnet + talc stability field

The prograde P-T evolution of the less retrograded sample US900 has been constrained using two different pseudosections calculated in the MnNCFMASHO model system, considering the fractionation effects due to the growth of garnet porphyroblasts: (i) a first pseudosection, calculated using the whole rock composition, has been used to model the growth of garnet core (Fig. 8a); (ii) a second pseudosection, calculated using the effective bulk composition derived by subtracting garnet cores and mantles to the whole rock composition, has been used to model the growth of garnet rim (Fig. 8b).

The topologies of both pseudosections are very similar. The observed talc + chloritoid + glaucophane + garnet assemblage is predicted to be stable in a quite small field. This field assemblage is limited toward lower pressure and temperature by the presence of chlorite instead of talc, toward higher pressure by the presence of carpholite instead of chloritoid and toward higher temperature by the presence of kyanite instead of chloritoid (Fig. S2); furthermore, it extends up to ca. 31 kbar, in the coesite-stability field (Fig. 8a,b). The dimension of the coesite + talc + chloritoid + glaucophane + garnet field assemblage is mainly controlled by the carpholite-in and kyanite-in trivariant reactions.

The position of the carpholite-in field boundary is critically dependent on the carpholite thermodynamic parameters used in the calculation; it is worth of note that the topology of Fig. 8a,b has been obtained using the most recent Holland & Powell (2011) database, whereas using older versions of the same database, the coesite + talc + chloritoid + glaucophane + garnet field assemblage is predicted to be stable in a narrower P-T field (Holland & Powell, 1998) or it is not predicted to be stable at all (Holland & Powell, 1998, updated 2004; i.e. the talc + chloritoid + glaucophane + garnet assemblage is only stable in the quartz stability field). The carpholite thermodynamic parameters and, consequently, its stability field, have been a matter of debate in the past (e.g. Vidal & Theye, 1996) and it is plausible that they are still not very well constrained. However, the results obtained using the Holland & Powell (2011) database are in very good agreement with the observed equilibrium assemblage and we are therefore confident that the thermodynamic parameters of carpholite are now quite well calibrated.

4.3 P-T evolution

The pseudosection calculated using the whole rock bulk composition allowed to constrain the P-T conditions for the growth of garnet core. Garnet core is predicted to grow in the quartz stability field, at T > 450 °C, through chlorite breakdown (Fig. 8a). The modelled garnet and chloritoid compositional isopleths [X_{Mg}(Grt)=0.08; X_{Ca}(Grt)=0.09; X_{Mn}(Grt)=0.12; X_{Mg}(Cld)=0.29] constrain the growth of garnet core at ca. 450-480°C, 22-26 kbar, in the chlorite + glaucophane + garnet + chloritoid + quartz + lawsonite field (lawsonite < 0.1 vol%; Fig. S2) (Fig. 8a). These temperature conditions are in very good agreement with the results obtained using the YAG thermometer (Pyle & Spear, 2000) applied on the maximum Y content measured in the garnet cores (i.e. 2000 ppm), which gives a maximum temperature of 496 °C.

P-T conditions for the growth of garnet rim have been constrained using the pseudosection calculated using the fractionated composition obtained by subtracting garnet cores and mantles to the whole rock bulk composition. The main differences between the two pseudosections is the shift of the garnet-in curve toward higher T and P for the fractionated pseudosection (Fig. 8b). The modelled garnet and chloritoid compositional isopleths [X_{Mg}(Grt)=0.20; X_{Ca}(Grt)=0.04; X_{Mn}(Grt)=0.00; X_{Mg}(Cld)=0.37] constrain the growth of garnet core at ca. 480-510°C, 25-31 kbar, in the talc + chloritoid + glaucophane + garnet + quartz/coesite field. The occurrence of coesite still preserved in garnet rim further constrain the P-T conditions of garnet rim at 480-510°C, 27-31 kbar (Fig. 8b). Finally, the modelled isomodes predicts the following modal abundances at the estimated peak P-T conditions: Coe36, Tlc29, Cld14, Gln12, Grt9 (vol%) (Fig. 8c-i), which are in very good agreement with the observed modal proportions of the main mineral phases.

Overall, the P-T evolution resulting from the thermodynamic modelling and thermometric results is characterized by a prograde increase in both pressure and temperature from ca. 460 °C, 25 kbar to ca. 510 °C, 28 kbar, just above the quartz to coesite transition (Fig. 9). The obtained results also suggest the crucial role of the quartz-consuming reaction Chl + Qz → Cld + Grt + Tlc for the formation of the observed equilibrium assemblage.

In sample US900, the retrogression effects are very scarce. The modelled H_2O isomodes show that, during exhumation, the system was H_2O under-saturated whatever decompression path was followed (either isobaric or cooling decompression) (Fig. 8l). This means that metamorphic reactions could not proceed until H_2O-saturated conditions were again reached or, alternatively, H_2O was introduced from outside (see Guiraud *et al*., 2001 for the interpretation of H_2O-saturated vs. H_2O-undersaturated conditions), and explains why the UHP assemblage remained preserved. On the opposite, in sample US773, chlorite pervasively grew at the expenses of chloritoid, glaucophane is locally rimmed by a discontinuous rim of NaCa-amphibole, and small epidote granoblasts occasionally occur in the rock matrix. This incipient retrogression can only be justified by the addition of a low H_2O amount from outside the system.

5. Discussion

5.1 Petrogenesis of the coesite-bearing chloritoid + garnet + glaucophane talcschists

The equilibrium assemblage observed in the studied rocks reflects a quite unusual Mg-rich composition that requires further discussion as concerning the possible protolith and the genetic processes involved in their formation. The studied talcschists can be described in a slightly oxidized MgO-FeO-Al_2O_3-SiO_2-H_2O system with low amounts of Na_2O (< 1 wt%) and CaO (< 0.3 wt%) (Table 3). They are not “whiteschist” *sensu stricto* because, according to the official nomenclature, they should contain the assemblage talc + kyanite (or the UHP equivalent pyrope + kyanite) (Fettes & Desmons, 2007), whereas the term “silvery micaschist”, used for similar chloritoid ± garnet ± phengite

353 talcschists can be applied (e.g. Compagnoni & Lombardo, 1974; Meffan-Main *et al*., 2004; Gabudianu
354 Radulescu *et al*., 2009). Beside the high amount of MgO, they are characterized by significant
355 amounts of FeO_{tot} (up to 16 wt%) and are completely devoid of K_2O (Table 3).
356 Possible protoliths with a composition suitable to develop the observed equilibrium
357 assemblage are: (1) Mg-rich rocks of either sedimentary or volcanic nature, and (2) metasomatically
358 altered felsic or mafic rocks (see Franz *et al*., 2013 for a discussion of the protoliths of whiteschists
359 and Ferrando, 2012 for a review on Mg-metasomatism of metagranitoids). The lack of field data and
360 of any information regarding the location of the ancient quarry from where these quern-stones were
361 extracted hampers a definitive interpretation of the protolith and of the genetic processes
362 responsible for the formation of the observed assemblage. However, because the site of the retrieval
363 of the quern-stones clearly points to a provenience of these rocks from the southern Dora-Maira
364 Massif, some speculations can be proposed.
365
366 ***5.1.1 Mg-rich protoliths metamorphosed in a closed-system***
367 Franz *et al*. (2013) demonstrated that pre- or syn-metamorphic metasomatism is not an essential
368 prerequisite for the formation of Mg-rich and alkali-poor assemblages. Both weathered or
369 hydrothermally altered volcanic rocks and Mg-rich sedimentary protoliths can have a composition
370 suitable to develop talc-bearing assemblages. Among sedimentary protoliths, the best candidates are
371 palygorskite-rich clays deposited in continental lacustrine or in shallow marine environments, and
372 sepiolite, illite and/or smectite-rich pelitic rocks from evaporitic successions deposited in
373 epicontinental marine settings (see also Kulke & Schreyer, 1976; Schreyer, 1977; Moine *et al*., 1981).
374 Although in principle a non-metasomatic origin cannot be excluded for the studied samples,
375 similar protoliths are unknown so far in the southern Dora-Maira Massif, which mainly consists of a
376 Variscan metamorphic basement (i.e. mainly amphibolite-facies metapelites with minor lenses of
377 metabasics and marbles) intruded by Permian granitoids.
378
379 ***5.1.2 Felsic or mafic protoliths metamorphosed in an open-system (i.e. metasomatic protoliths)***
380 Although the chemical weathering could be locally responsible for the Mg-metasomatism of the
381 protolith of a HP-UHP rock (e.g., Franz *et al*., 2013), in an orogenic setting such as the Alps many
382 other pervasive Mg-metasomatic processes widely occur and are more suitable to produce small
383 volumes (layers, lens-like bodies, veins, etc.) of Mg-metasomatic rocks. Ferrando (2012) discussed
384 the metasomatic processes responsible for the transformation of alkali-rich metagranitoids into Mg-
385 rich and alkali-poor metasomatic schists in the Alps, and demonstrated that these processes were
386 widespread and can be ascribed to different tectonic settings that were active at different times.
387 From this review, the most common Mg-metasomatic process that affected the continental crustal
388 rocks of the Alps along shear zones results to be the pervasive influx of Mg-rich, highly channelized
389 fluids derived from ultramafics previously interacting with seawater. This process can occur during
390 the rift-related ocean-continent transition, the continental subduction and/or the continent–
391 continent collision. The metasomatic products are typically characterized by strong depletions in
392 alkalis (very low or even null K_2O and Na_2O contents) and low depletions in silica, and by strong
393 enrichments in MgO (+ minor NiO_2 and/or Cr_2O_3) and by variable enrichments in FeO_{tot} depending on
394 the initial composition of the protolith. Mg-metasomatic rocks formed at the expenses of granitic
395 protoliths (e.g. the well-known pyrope-bearing whiteschists of the Brossasco-Isasca Unit; Ferrando *et*
396 *al*., 2009) are low in FeO_{tot} (< 2 wt%), whereas those formed at the expenses of granodioritic
397 protoliths are significantly richer in FeO_{tot}. For example, chlorite + garnet + staurolite schists (almost
398 free of quartz) with up to ca. 19 wt% of FeO_{tot}, but with low Na_2O (< 0.5 wt%) and SiO_2 (< 32 wt%)

and relatively high CaO (> 0.7 wt%) and K_2O (> 3.5 wt%), are described as the final metasomatic product of a metagranodiorite from the Tauern window of eastern Alps (Selverstone *et al*., 1991; Barnes *et al*., 2004).

Meyer *et al*. (2014) described coesite-bearing garnet + chloritoid talcschists with mineral assemblage and compositions similar to those described in this study, but with a significantly lower modal amount of quartz (< 5 vol%) and lacking of glaucophane. Because the field evidence shows that the talcschists envelop blocks and boudins of mafic oceanic rocks tectonically embedded in continentally derived metasediments, these Authors interpreted the talcschists as the metasomatic product of a mafic protolith (either hydrothermally altered oceanic crust or volcaniclastic rock). Also these talcschists are characterized by high FeO_{tot} contents (FeO_{tot} = 20 wt%) and very low alkalis, but show a low SiO_2 content (45 wt%).

Both these two protoliths, i.e. granitoids and strongly altered mafic rocks, can be reasonably excluded for the studied rocks. The studied talcschists cannot derive from a Fe-rich metagranitoid, i.e. a metagranodiorite, because the amounts of Na_2O and SiO_2 are too high and those of CaO and K_2O are too low compared with the previously documented examples of metasomatic granodiorites (Selverstone *et al*., 1991; Barnes *et al*., 2004). Moreover, metagranodiorites, or chemically equivalent orthogneisses, are not reported in the southern Dora-Maira Massif (e.g. Compagnoni *et al*., 2012 and references therein). Similarly, a protolith consisting of altered oceanic crust or altered volcaniclastic rocks, is not compatible with the bulk of the studied rocks and is not coherent with the tectonic setting of the southern Dora-Maira Massif (e.g. Compagnoni *et al*., 2012).

One of the quern-stone associated to those carved from the talcschists is carved from a garnet + chloritoid + glaucophane phengitic schist (Fig. S3), i.e. a widespread lithology outcropping in the Rocca-Solei Unit (e.g. Compagnoni & Rolfo, 2003; Compagnoni *et al*., 2012). Although we cannot prove that this quern-stone was extracted from the same locality of the studied coesite + chloritoid + garnet ± glaucophane talcschists, we can speculate that this lithology might represent the most credible non-metasomatized equivalent of the talcschists. If it is the case, the Mg-metasomatism could have moderately affected a “common” Fe-rich metapelite such as those that constitute the majority of the Variscan basement in the southern Dora-Maira Massif.

Regarding the kind of metasomatism and its timing, the relatively high Cr content in garnet points to the involvement of mantle derived fluids, and both microstructural relationships and minerochemical data point to a process occurred before the garnet growth (i.e. at P < 25 kbar). In fact, the Cr concentration decreases from garnet core to rim (Fig. 6b), opposite to what would be expected if a Mg-rich, mantle derived, metasomatic fluid was introduced in the system after the growth of garnet core (e.g. Ferrando *et al*., 2009). This implies that the metasomatic process could have occurred during early subduction, such as occurred for the well-known pyrope-bearing whiteschists in the UHP Brossasco-Isasca Unit (Ferrando *et al*., 2009), i.e. by a prograde influx of antigorite-derived fluids along shear zones. However, as an alternative process, the metasomatism could have occurred during the opening of the Tethyan basin, when fluids derived from hydrated ultramafic rocks could have infiltrated the continental crust along rift-related detachment systems (Ferrando, 2012).

5.2 Possible evidence for a new UHP unit in the southern Dora-Maira Massif

The location of the *villa rustica* and the occurrence of coesite relics, might have suggested the obvious conclusion that the studied talcschists come from the nearby UHP Brossasco-Isasca Unit (BIU), which is only ca. 5 km from Costigliole Saluzzo (Fig. 1a). However, the results of thermodynamic modelling clearly show that the studied talcschists experienced peak P-T conditions

at UHP conditions, but at significant lower temperature (and pressure) than the BIU (Fig. 9). In the western Alps, the only other UHP unit known so far is the Lago di Cignana Unit (e.g. Reinecke, 1991; Groppo *et al*., 2009; Frezzotti *et al*., 2011), located in the Internal Piemontese Zone (Zermatt-Saas Zone) of the upper Valtournanche, ca. 150 km from Costigliole Saluzzo. The calculated P-T conditions for the prograde and peak stages do not match with the P-T path obtained for the Lago di Cignana Unit (Groppo *et al.*, 2009) and it can be, therefore, excluded that the quern-stones come from there.

The high number of quern-stones carved from garnet + chloritoid + glaucophane talcschist and phengitic schists unearthed in the *villa rustica* suggests that they were not realized starting from a small outcrop or block occasionally found in the surroundings, but that a small quarry should have existed, likely set in correspondence of a talcschist horizon (thick at least few meters and with a good lateral continuity) possibly within the phengitic schists of the Rocca-Solei Unit. Coesite relics have been never reported so far from this Unit; however, the Rocca-Solei Unit has been significantly less studied than the BIU (the last petrological works date back to more than 15 years ago: Chopin *et al*., 1991; Matsumoto & Hirajima, 2000) and it is possible that a systematic search for UHP evidence could led to new coesite findings in the next future.

Further fieldwork and petrological investigation are therefore required in order to confirm (or disprove) the existence of a second UHP unit in the southern Dora-Maira Massif. Such a discovery could potentially have important implications for the understanding of the subduction and exhumation processes that were active in convergent settings and that were responsible for the actual architecture of the Alpine chain.

Acknowledgements

We gratefully acknowledge Roberto Compagnoni for being a constant source of inspiration and for sharing his longstanding experience: we are indebted to him for most of our knowledge about the southern Dora-Maira Massif.

Raman analytical facilities were provided by the Interdepartmental Center “G. Scansetti” and by the Compagnia di San Paolo, Torino, Italy.

References

Barnes, J.D., Selverstone, J., Sharp, Z.D. (2004): Interactions between serpentinite devolatilization, metasomatism and strike-slip strain localization during deep-crustal shearing in the Eastern Alps. *J. Metamorph. Geol*., **22**, 283–300.

Bosse, V., Ballevre, M., Vidal, O. (2002): Ductile thrusting recorded by the garnet isograd from blueschist-facies metapelites of the Ile de Groix, Armorican Massif, France. *J. Petrol*., **43**, 485–510.

Castelli, D., Compagnoni, R., Lombardo, B. Angiboust, S., Balestro, G., Ferrando, S., Groppo, C., Hirajima, T., Rolfo, F. (2014): Crust-mantle interactions during subduction of oceanic & continental crust. 10th International Eclogite Conference, Courmayeur (Aosta, Italy): Post-conference excursions: September 9-10, 2013. *Geological Field Trips*, **6 (1.3)**, 73 pp.

Chopin, C., Henry, C., Michard, A. (1991): Geology and petrology of the coesite-bearing terrain, Dora Maira massif, Western Alps. *Eur. J. Mineral*., **3**, 263–291.

Chopin, C. & Monié, P. (1984): A unique magnesiochloritoid-bearing, high-pressure assemblage from the Monte Rosa, Western Alps: petrologic and $^{40}Ar/^{39}Ar$ radiometric study. *Contrib. Mineral. Petrol*., **87**, 388–398.

Chopin, C. (1981): Talc-phengite: a widespread assemblage in high-grade pelitic blueschists of the Western Alps. *J. Petrol*., **22**, 628–650.

Compagnoni, R. & Rolfo, F. (2003): Ultrahigh-pressure units in the Western Alps. *in*: "Ultrahigh-pressure metamorphism", D.A. Carswell & R. Compagnoni, eds., EMU Notes in Mineralogy, 5, 13–49.

Compagnoni, R., Rolfo, F., Groppo, C., Hirajima, T., Turello, R. (2012): Geologic map of the UHP Brossasco-Isasca Unit (Western Alps). *J. Maps*, **8**, 465–472.

Compagnoni, R. & Lombardo, B. (1974): The Alpine age of the Gran Paradiso eclogites. *Rend. Soc. It. Mineral. Petrol*., **30**, 223–237.

Connolly, J.A.D. (2009): The geodynamic equation of state: what and how. *Geochem. Geophys. Geosyst*., **10**, Q10014.

Connolly, J.A.D. (1990): Multivariable phase diagrams: an algorithm based on generalized thermodynamics. *Am. J. Sci*., **290**, 666–718.

Cossio, R., Borghi, A., Ruffini, R. (2002): Quantitative modal determination of geological samples based on X-ray multielemental map acquisition. *Microsc. Microanal*., **8**, 139–149.

Dal Piaz, G. & Lombardo, B. (1986): Early Alpine eclogite metamorphism in the Penninic Monte Rosa-Gran Paradiso basement nappes of the northwestern Alps. *Geol. Soc. Am. Bull.*, **164**, 249–265.

Dale, J., Holland, T., Powell, R. (2000): Hornblende-garnet-plagioclase thermobarometry: a natural assemblage calibration of the thermodynamics of hornblende. *Contrib. Mineral. Petrol*., **140**, 353–362.

Diener, J.F.A. & Powell R. (2011): Revised activity–composition models for clinopyroxene and amphibole. *J. Metamorph. Geol*., **30**, 131–142.

Donner, M. & Marzoli, C. (1994): La macinazione. Evoluzione delle tecniche e degli strumenti. *In:* "Il grano e le macine: la macinazione di cereali in Alto Adige, dall'Antichità al Medioevo", S. de Rachewiltz, L. Dal Ri, C. Marzoli, eds., Castel Tirolo, 73-93.

Elia, D. & Meirano, V. (2012): La villa di Costigliole Saluzzo (CN). Contributo alla conoscenza del territorio piemontese in età romana. *Orizzonti. Rassegna di Archeologia*, **XIII,** 43–65.

Elia, D., Meirano, V., Russo, D. (2013): Costigliole Saluzzo, località Cimitero. Insediamento di età romana. Interventi di scavo e di restauro: campagna 2012. *Quaderni della Soprintendenza Archeologica del Piemonte*, **28**, 220–223.

El-Shazly, A.E.D.K. & Liou, J.G. (1991): Glaucophane-chloritoid-bearing assemblages from NE Oman: petrologic significance and petrogenetic grid for high P metapelites. *Contrib. Mineral. Petrol*., **107**, 180–201.

Ferrando, S. (2012): Mg-metasomatism of metagranitoids from the Alps: genesis and possible tectonic scenarios. *Terra Nova*, **24**, 423 *Contrib. Mineral. Petrol*., 436.

Ferrando, S., Frezzotti, M.L., Petrelli, M., Compagnoni, R. (2009): Metasomatism of continental crust during subduction: the UHP whiteschists from the Southern Dora-Maira Massif (Italian Western Alps). *J. Metamorph. Geol*., **27**, 739–756.

Fettes, D. & Desmons, J. (2007): Metamorphic rocks. A Classification and Glossary of Terms. Recommendations of the International Union of Geological Sciences Subcommission on the Systematics of Metamorphic Rocks. Cambridge University Press, Cambridge, 244 pp.

Franz, L., Romer, R.L., de Capitani, C. (2013): Protoliths and phase petrology of whiteschists. *Contrib. Mineral. Petrol*., **166**, 255–274.

Frezzotti, M.L., Selverstone, J., Sharp, Z.D., Compagnoni, R. (2011): Carbonate dissolution during subduction revealed by diamond-bearing rocks from the Alps. *Nat. Geosci*., **4**, 703–706.

Frezzotti, M.L., Tecce, F., Casagli, A. (2011): Raman spectroscopy for fluid inclusion analysis. *J. Geochem. Explor.*, **112**, 1-20.

Gabudianu Radulescu, I., Rubatto, D., Gregory, C., Compagnoni, R. (2009): The age of HP metamorphism in the Gran Paradiso Massif, Western Alps: a petrological and geochronological study of ‘‘silvery micaschists’’. *Lithos*, **110**, 95–108.

Ghent, E.D., Stout, M.Z., Black, P.M., Brothers, R.N. (1987): Chloritoid-bearing rocks associated with blueschists and eclogites, northern New Caledonia. *J. Metamorph. Geol*., **5**, 239–254.

Goffé, B. & Chopin, C. (1986): High-pressure metamorphism in the Western Alps: zoneography of metapelites, chronology and consequences. *Schweiz. Mineral. Petrog. Mitt*., **66**, 41–52.

Groppo, C., Beltrando, M., Compagnoni, R. (2009): P-T path of the UHP Lago di Cignana and adjoining HP meta-ophiolitic units: insights into the evolution of subducting tethyan slab. *J. Metamorph. Geol*., **27**, 207–231.

Guiraud, M., Burg, J.P., Powell, R. (1987): Evidence for a Variscan suture zone in the Vendée, France: a petrological study of blueschist facies rocks from Bois de Cene. *J. Metamorph. Geol*., **5**, 225–237.

Guiraud, M., Holland, T., Powell, R. (1990): Calculated mineral equilibria in the greenschist-blueschist-eclogite facies in Na_2O-FeO-MgO-Al_2O_3-SiO_2-H_2O. *Contrib. Mineral. Petrol*., **104**, 85–98.

Guiraud, M., Powell, R., Rebay, G. (2001): H_2O in metamorphism and unexpected behaviour in the preservation of metamorphic mineral assemblages. *J. Metamorph. Geol*., **19**, 445–454.

Holland, T.J.B. & Powell, R. (2011): An improved and extended internally consistent thermodynamic dataset for phases of petrological interest, involving a new equation of state for solids. *J. Metamorph. Geol*., **29**, 333–383.

Holland, J.T.B., Baker, J., Powell, R. (1998): Mixing properties and activity-composition relationships of chlorites in the system MgO-FeO-Al_2O_3-SiO_2-H_2O. *Eur. J. Mineral*., **10**, 395–406.

Katagas, C. (1980): Ferrograucophane and chloritoid-bearing metapelites from the phylitte series, southern Peloponnese, Greece. *Mineral. Mag*., **43**, 975–978.

Kiénast, J.R. & Triboulet, C. (1972): Le chloritoide dans les paragenèses à glaucophane, albite ou paragonite. *Bull. Soc. Franc. Minéral. Cristall*., **95**, 565–573.

Klemd, R., Gao, J., Li, J.-L., Meyer, M. (2015): Metamorphic evolution of (ultra)-high-pressure subduction-related transient crust in the South Tianshan Orogen (Central Asian Orogenic Belt): Geodynamic implications. *Gondw. Res*., **28**, 1–25.

562 Kohn, M.J. (2014): “Thermoba-Raman-try”:Calibration of spectroscopic barometers and
563 thermometers for mineral inclusions. *Earth Planet. Sci. Lett.*, **388**, 187-196.
564 Korsakov, A.V., Hutsebaut, D., Theunissen, K., Vandenabeele, P., Stepanov, A.S. (2007): Raman
565 mapping of coesite inclusions in garnet from the Kokchetav Massif (Northern Kazakhstan).
566 *Spectrochim. Acta Part A*, **68**, 1046-1052.
567 Korsakov, A.V., Perraki, M., Zhukov, V.P., De Gussem, K., Vandenabeele, P., Tomilenko, A.A. (2009): Is
568 quarts a potential indicator of ultrahigh-pressure metamorphism? Laser Raman spectroscopy of
569 quartz inclusions in ultrahigh-pressure garnets. *Eur. J. Mineral.*, **21**, 1313-1323.
570 Kulke, H. & Schreyer, W. (1973): Kyanite–talc–schist from Sar E Sang, Afghanistan. *Earth Planet. Sci.*
571 *Lett*., **18**, 324–328.
572 Lopez-Carmona, A., Abati, J., Reche, J. (2010): Petrologic modeling of chloritoid–glaucophane schists
573 from the NW Iberian Massif. *Gondw. Res*., **17**, 377–391.
574 Matsumoto, N. & Hirajima, T. (2000): Garnet in pelitic schists from a quartz-eclogite unit in the
575 southern Dora-Maira massif, Western Alps. *Schweiz. Mineral. Petrog. Mitt*., **80**, 55–62.
576 Meffan-Main, S., Cliff, R.A., Barnicoat, A.C., Lombardo, B., Compagnoni, R. (2004): A tertiary age for
577 Alpine high pressure metamorphism in the Gran Paradiso massif, Western Alps: a Rb-Sr
578 microsamplimg study. *J. Metamorph. Geol*., **22**, 267–281.
579 Meyer, M., Klemd, R., Hegner, E., Konopelko, D. (2014): Subduction and exhumation mechanisms of
580 ultra-high and high-P oceanic and continental crust at Makbal (Tianshan, Kazakhstan and
581 Kyrgyzstan). *J. Metamorph. Geol*., **32**, 861–884.
582 Miyazaki, K., Zulkarnain, I., Sopaheluwakan, J., Wakita, K. (1996): Pressure-temperature conditions
583 and retrograde paths of eclogites, garnet-glaucophane rocks and schists from South Sulawesi,
584 Indonesia. *J. Metamorph. Geol*., **14**, 549–563.
585 Moine, B., Sauvan, P., Jarousse, J. (1981): Geochemistry of evaporitic-bearing series: a tentative guide
586 for the identification of metaevaporites. *Contrib. Miner. Petrol*., **76**, 401–412.
587 Newton, R.C., Charlu, T.V., Kleppa, O.J. (1980): Thermochemistry of the high structural state
588 plagioclases*. Geoch. Cosmoch. Acta*, **44**, 933–941.
589 Okay, A.I. (2002): Jadeite-chloritoid-glaucophane-lawsonite blueschists from north-west Turkey:
590 unusually high P/T ratios in continental crust. *J. Metamorph. Geol*., **20**, 757–768.
591 Orozbaev, R., Hirajima, T., Bakirov, A., Takasu, A., Maki, K., Yoshida, K., Sakiev, K., Bakirov, A., Hirata,
592 T., Tagiri, M., Togonbaeva, A. (2015): Trace element characteristics of clinozoisite pseudomorphs
593 after lawsonite in talc-garnet-chloritoid schists from the Makbal UHP Complex, northern Kyrgyz
594 Tian-Shan. *Lithos*, **226**, 98–115.
595 Pouchou, J.L. & Pichoir, F. (1988): Determination of mass absorption coefficients for soft X-Rays by
596 use of the electron microprobe. Microbeam Analysis, San Francisco Press, pp 319–324.
597 Proyer, A. (2003): Metamorphism of pelites in NKFMASH - a new petrogenetic grid with implications
598 for the preservation of high pressure mineral assemblages during exhumation. *J. Metamorph.*
599 *Geol*., **21**, 493–509.
600 Pyle, J.M. & Spear, F.S. (2000): An empirical garnet (YAG) ± xenotime thermometer. *Contrib. Mineral.*
601 *Petrol*., **138**, 51–58.
602 Reinecke, T. (1991): Very-high pressure metamorphism and uplift of coesite-bearing metasediments
603 from the Zermatt-Saas zone, Western Alps. *Eur. J. Mineral*., **3**, 7–17.
604 Schreyer, W. (1977): Whiteschists: their compositions and pressure–temperature regimes based on
605 experimental, field and petrographic evidence. *Tectonophysics*, **34**, 127–144.

606 Selverstone, J., Morteani, G., Staude, J.M. (1991): Fluid channelling during ductile shearing:
607 transformation of granodiorite into aluminous schist in the Tauren Window, Eastern Alps. J.
608 *Metamorph. Geol*., **9**, 419–431.
609 Smye, A.J., Greenwood, L.V., Holland, T.J.B. (2010): Garnet–chloritoid–kyanite assemblages: eclogite
610 facies indicators of subduction constraints in orogenic belts. *J. Metamorph. Geol*., **28**, 753–768.
611 Theye, T. & Seidel, E. (1991): Petrology of low-grade high pressure metapelites from the External
612 Hellenides (Crete, Peloponnese). A case study with attention to sodic minerals. *Eur. J. Mineral*., **3**,
613 343–366.
614 Vidal, O. & Theye, T. (1996): Petrology of Fe-Mg-carpholite-bearing metasediments from NE Oman. *J.*
615 *Metamorph. Geol*., **14**, 381–397.
616 Warren, C.J. & Waters, D.J. (2006): Oxidized eclogites and garnet-blueschists from Oman: P–T path
617 modelling in the NCFMASHO system. *J. Metamorph. Geol*., **24**, 783–802.
618 Wei, C., Wang, W., Clarke, G.L., Zhang, L., Song, S. (2009): Metamorphism of high/ultrahigh-pressure
619 pelitic-felsic schist in the South Tianshan Orogen, NW China: phase equilibria and P-T path. *J.*
620 *Petrol*., **50**, 1973–1991.
621 Wei, C.J. & Powell, R. (2004): Calculated phase relations in high-pressure metapelites in the system
622 NKFMASH (Na_2O–K_2O–FeO–MgO–Al_2O_3–SiO_2–H_2O) with application to natural rocks. *J. Petrol*., **44**,
623 183–202.
624 Wei, C.J. & Powell, R. (2006): Calculated phase relations in the system NCKFMASH (Na_2O-CaO-K_2O-
625 FeO-MgO-Al_2O_3-SiO_2-H_2O) for high-pressure metapelites. *J. Petrol*., **47**, 385–408.
626 Wei, C.J. & Song, SG. (2008): Chloritoid-glaucophane schist in the north Qilian orogen, NW China:
627 phase equilibria and P-T path from garnet zonation. *J. Metamorph. Geol*., **26**, 301–316.
628 White, R., Pomroy, N., Powell, R. (2005): An in-situ metatexite– diatexite transition in upper
629 amphibolite facies rocks from Broken Hill, Australia. *J. Metamorph. Geol*., **23**, 579–602.
630 Whitney, D.L. & Evans, B.W. (2010): Abbreviations for names of rock-forming minerals. *Am. Mineral*.,
631 **95**, 185–187.
632

Figure captions

Fig. 1 – **(a)** Tectonic sketch map of the southern Dora-Maira Massif, with the location of Costigliole Saluzzo (modified from Castelli *et al*., 2014). **(b)** The roman villa at Costigliole Saluzzo (from Elia *et al*., 2013; in red: room H2, where the majority of the querns come from). **(c)** A quern stone during its excavation.

Fig. 2 – **(a, b)** Rotary querns from Costigliole Saluzzo (a: specimen from US900; b: specimen from US773). **(c)** Reconstruction of a quern (from Donner & Marzoli, 1994) **(d, e, f)** Details of specimens from US773 (d), US900 (e) and US557 (f).

Fig. 3 – Processed major elements μ-XRF maps of the whole thin sections of samples US900 and US773.

Fig. 4 – **(a, b)** Representative microstructures of samples US900 (a) and US773 (b) (Plane Polarized Light: PPL). **(c, d)** Garnet porphyroblasts with coesite (partially inverted to quartz) inclusion in the rim and chloritoid inclusion in the core (c: US900; d: US773) (PPL). **(e)** Zoned glaucophane nematoblasts associated to blue-green chloritoid (US900) (PPL). **(f)** Sligthly zoned blue-green chloritoid partially replaced by greenish Mg-chlorite (US773) (PPL). Mineral abbreviations after Whitney & Evans (2010).

Fig. 5 – **(a-c)** Glaucophane composition plotted in the Si vs. $Mg/(Mg+Fe^{+2})$ (a), Si vs. Fe^{+3}/Fe_{tot}, and Si vs. Na/(Na+Ca) diagrams (data from both samples US900 and US773). **(d)** Chloritoid composition plotted in the $(Fe^{+2}+Mg)$-$(Al^{VI}+Fe^{+3})$-Mg diagram (data from both samples US900 and US773).

Fig. 6 – **(a)** Garnet composition plotted in the Prp-Alm-(Sps+Grs) diagram (data from both samples US900 and US773). **(b)** Major and trace element chemical profile of a garnet porphyroblast from sample US900. Note the bell shaped profile of X_{Mn}, suggesting a prograde growth and the similar pattern of Y, Na and Cr.

Fig. 7 – **(a)** Microphotograph of large and relatively well preserved coesite inclusion within garnet mantle, and smaller polycrystalline quartz inclusions within garnet rim (US773; crossed polarized light). **(b)** Microphotograph of relatively small coesite inclusion, partly inverted to palisade quartz, within garnet rim (US773) (PPL). **(c)** Raman spectrum of coesite (US773). **(d)** Microphotograph of the mapped, well preserved coesite inclusion in garnet. The rectangle shows the mapped area reported in Fig. 7e (US773) (PPL). **(d)** Raman map of the spatial distribution and the intensity of the main peaks of coesite (524 cm^{-1}, in green), quartz (470 cm^{-1}, in blue), and garnet (917 cm^{-1}, in red). From the map is evident that the coesite inversion to quartz start from the grain-boundaries and the fractures.

Fig. 8 – **(a)** P-T pseudosection calculated for sample US900 in the MnNCFMASH system using the whole rock bulk composition (Table 3). The variance of the fields varies from three (i.e. 7 phases, light grey fields) to six (i.e. 4 phases, darker grey fields). Pink continuous, dashed and dotted lines are the X_{Mg}, X_{Ca} and X_{Mn} isopleths of garnet corresponding to the measured composition of garnet core; light blue continuous line is the X_{Mg} isopleth of chloritoid corresponding to the measured composition of chloritoid core. P-T conditions constrained for the growth of garnet core are represented by the white dotted polygon. **(b)** P-T pseudosection calculated for sample US900 using

678 the fractionated bulk composition (whole rock composition minus garnet core and mantle; Table 3).
679 The variance of the fields varies from three (i.e. 7 phases, light grey fields) to six (i.e. 4 phases, darker
680 grey fields). Pink continuous, and dashed lines are the X_{Mg} and X_{Ca} isopleths of garnet corresponding
681 to the measured composition of garnet rim; light blue continuous line is the X_{Mg} isopleth of chloritoid
682 corresponding to the measured composition of chloritoid rim. P-T conditions constrained for the
683 growth of garnet rim are represented by the white dotted polygon. **(c-l)** Modal variations (vol%) of
684 the main mineral phases in sample US900 (c-i) and isomodes of water (mol) (l) calculated for the P-T
685 pseudosection of Fig. 8b. Colours from blue to red imply higher modal proportions as indicated in
686 each legend. The black arrow is the prograde P-T path constrained basing on the pseudosection
687 results and YAG thermometry.
688
689 **Fig. 9** – Prograde P-T path (black arrow) inferred for the studied samples basing on the
690 pseudosection results and YAG thermometry and comparison with the P-T evolution constrained for
691 the adjacent UHP Brossasco-Isasca Unit (dashed grey arrow). The blue and light blue polygons
692 represent the P-T conditions constrained for the growth of garnet core and rim, respectively (see Fig.
693 8a, b).
694
695
696

Figure 1
Click here to download Figure: Fig1.tif

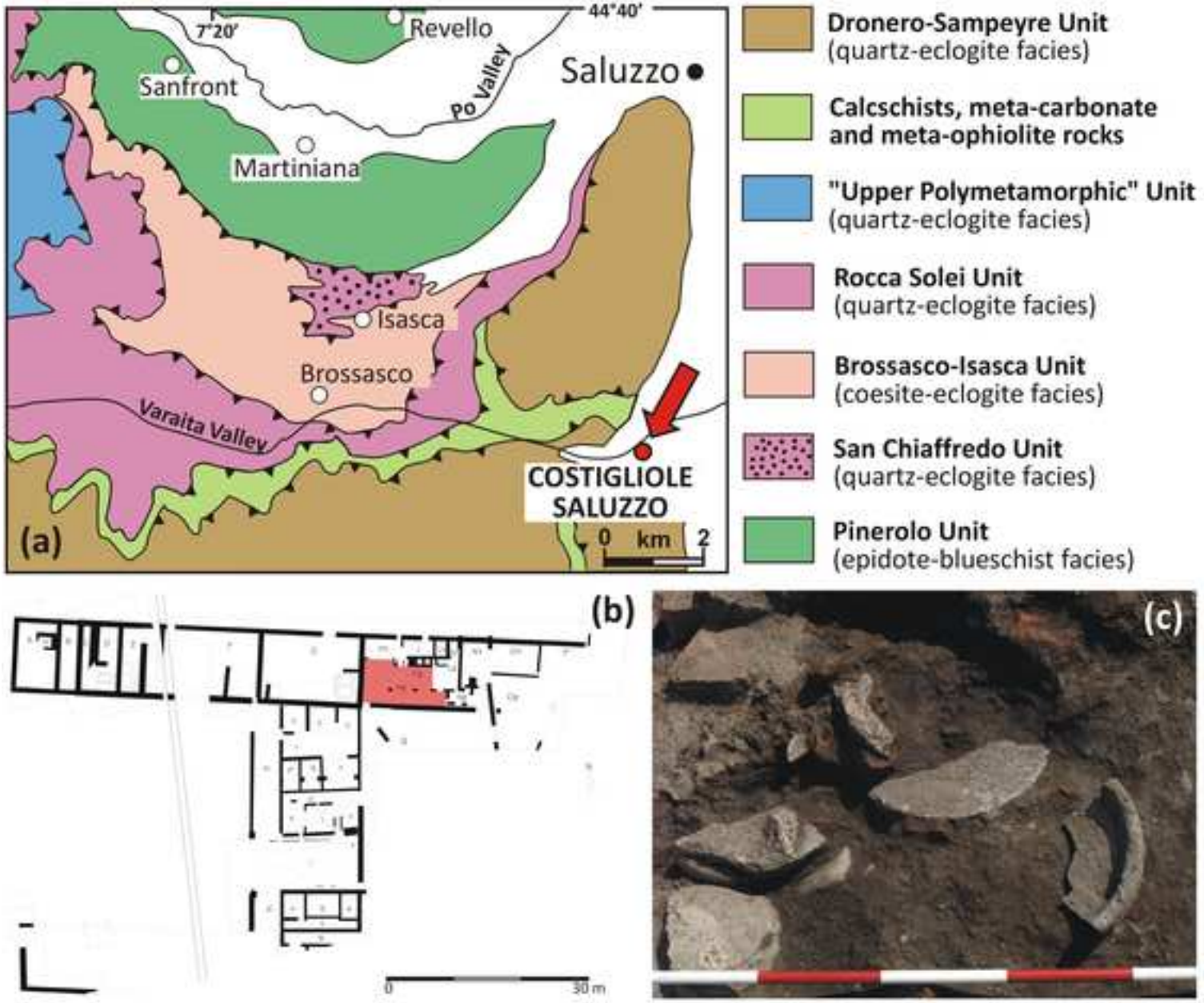

Fig. 1 (a) Tectonic sketch map of the southern Dora-Maira Massif, with the location of Costigliole Saluzzo (modified from Castelli *et al.*, 2014). (b) The roman villa at Costigliole Saluzzo (from Elia *et al.*, 2013; in red: room H2, where the majority of the querns come from). (c) A quern stone during its excavation.

Figure 2
Click here to download Figure: Fig2.tif

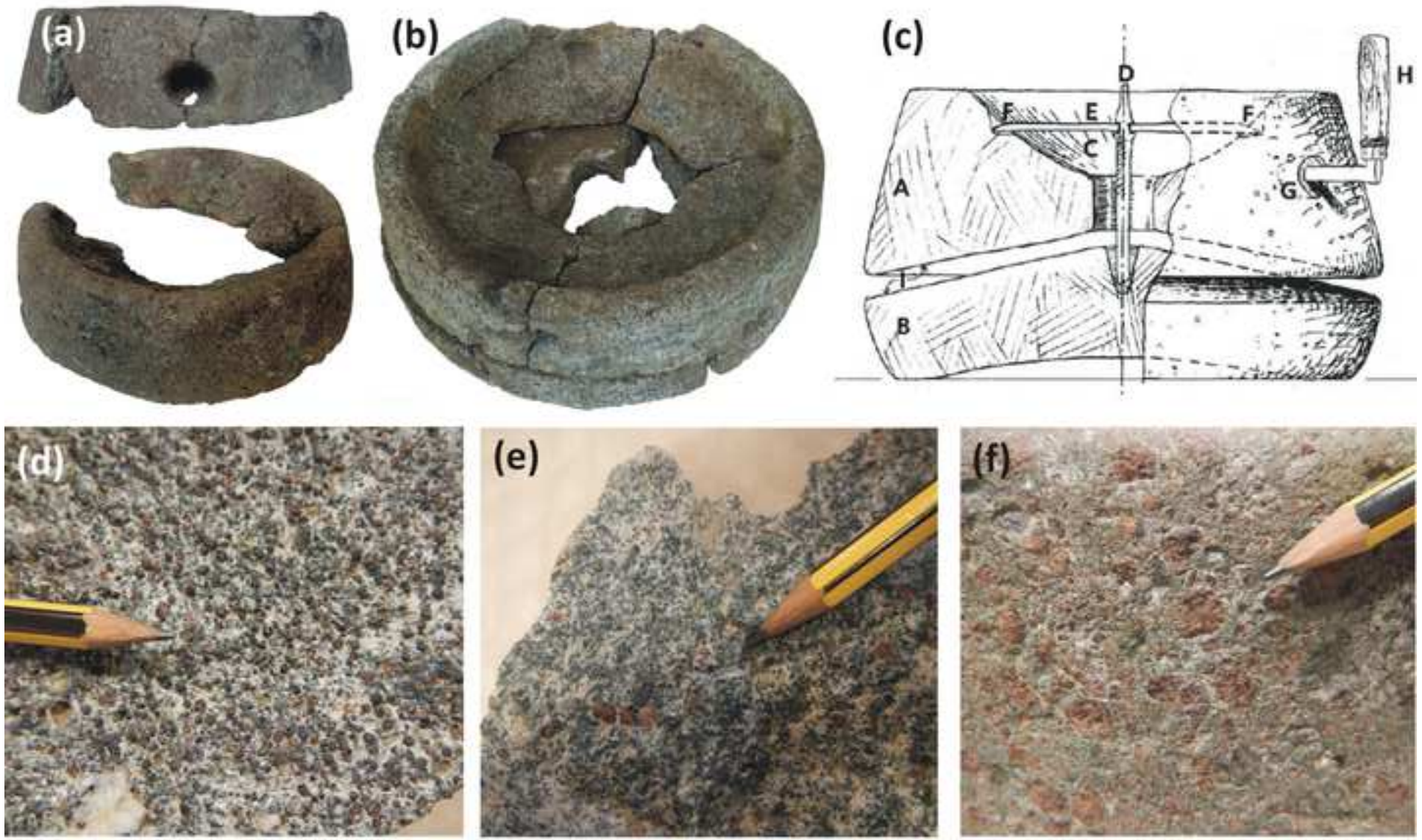

Fig. 2 **(a, b)** Rotary querns from Costigliole Saluzzo (a: specimen from US900; b: specimen from US773). **(c)** Reconstruction of a quern (from Donner & Marzoli, 1994) **(d, e, f)** Details of specimens from US773 (d), US900 (e) and US557 (f).

Figure 3
Click here to download Figure: Fig3.tif

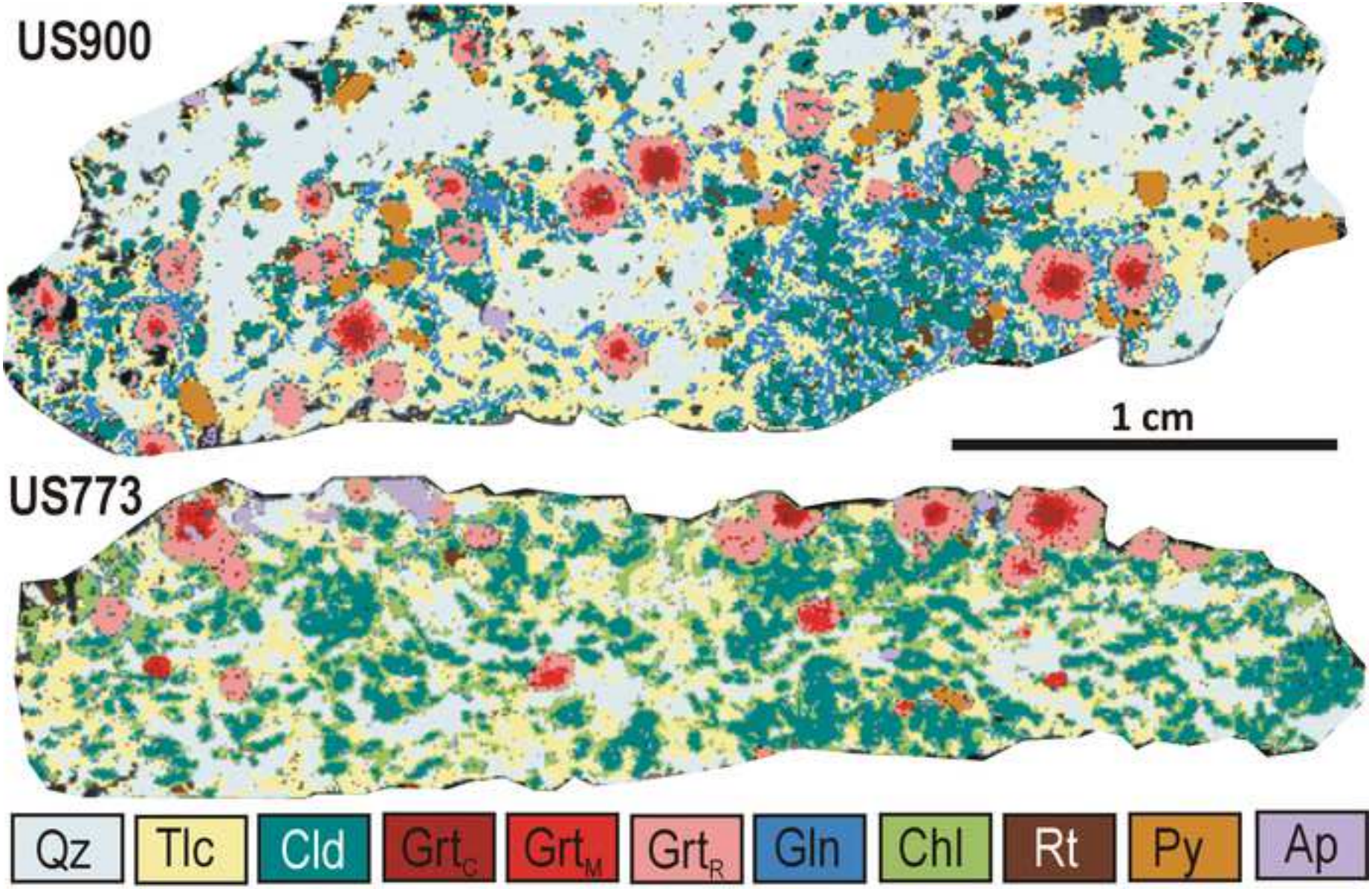

Fig. 3 Processed major elements μ-XRF maps of the whole thin sections of samples US900 and Us773.

Figure 4
Click here to download Figure: Fig4.tif

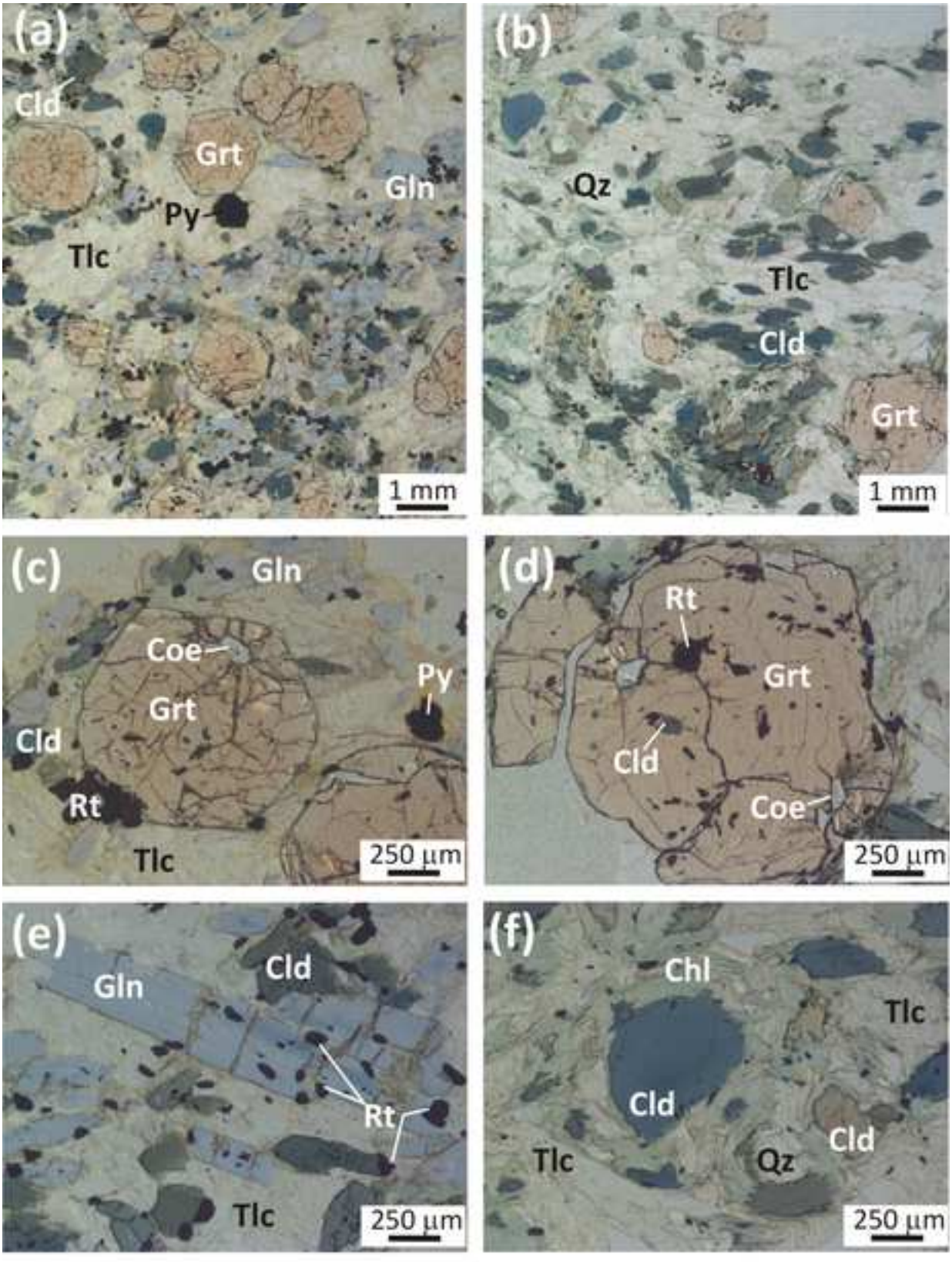

Fig. 4 **(a, b)** Representative microstructures of samples US900 (a) and US773 (b) (Plane Polarized Light: PPL). **(c, d)** Garnet porphyroblasts with coesite (partially inverted to quartz) inclusion in the rim and chloritoid inclusion in the core (c: US900; d: US773) (PPL). **(e)** Zoned glaucophane nematoblasts associated to blue-green chloritoid (US900) (PPL). **(f)** Slighly zoned blue-green chloritoid partially replaced by greenish Mg-chlorite (US773) (PPL). Mineral abbreviations after Whitney & Evans (2010).

Figure 5
Click here to download Figure: Fig5.tif

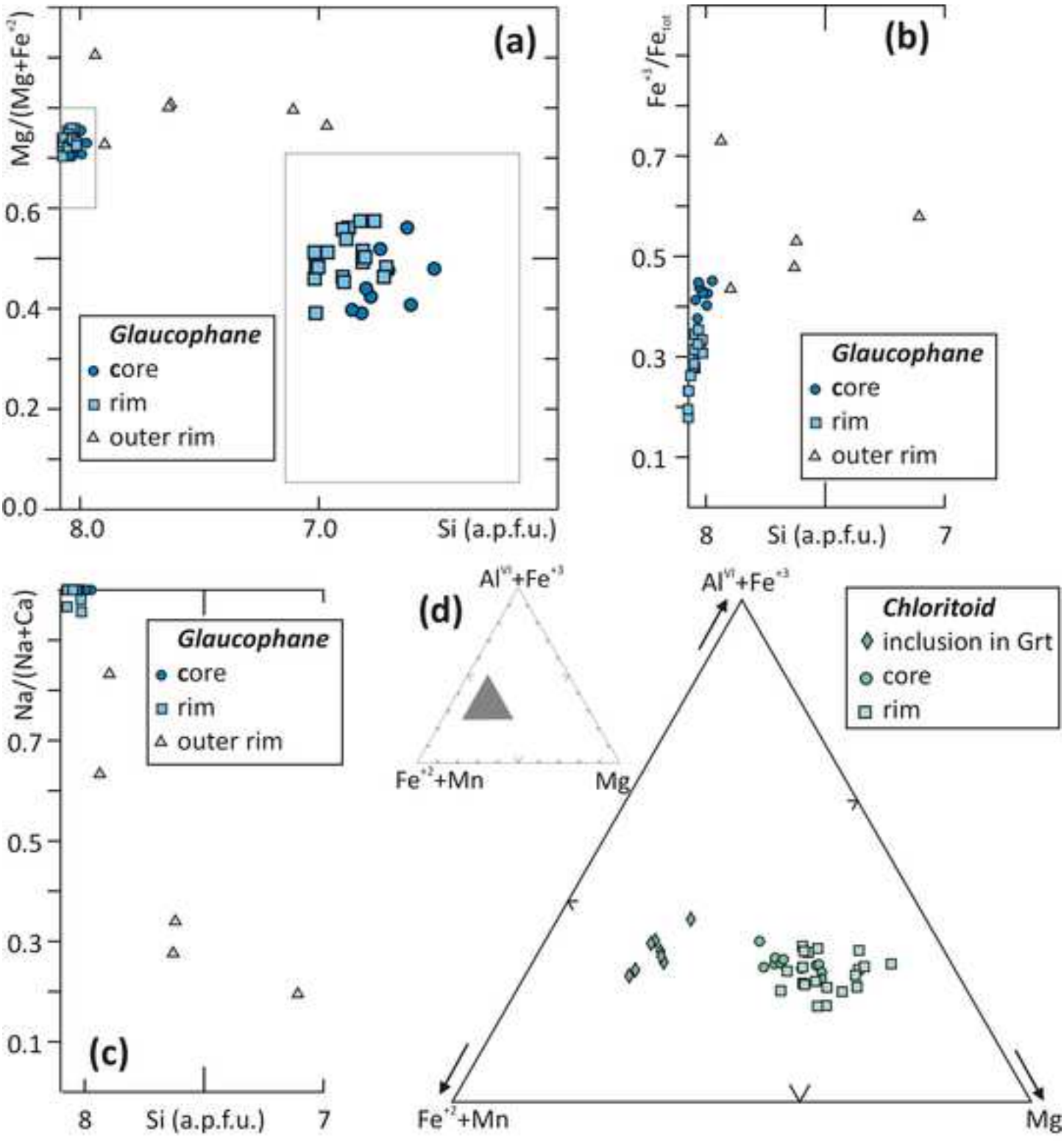

Fig. 5 (a-c) Glaucophane composition plotted in the Si vs. $Mg/(Mg+Fe^{+2})$ (a), Si vs. Fe^{+3}/Fe_{tot}, and Si vs. Na/(Na+Ca) diagrams (data from both samples US900 and US773). **(d)** Chloritoid composition plotted in the $(Fe^{+2}+Mg)$-$(Al^{VI}+Fe^{+3})$-Mg diagram (data from both samples US900 and Us773).

Figure 6
Click here to download Figure: Fig6.tif

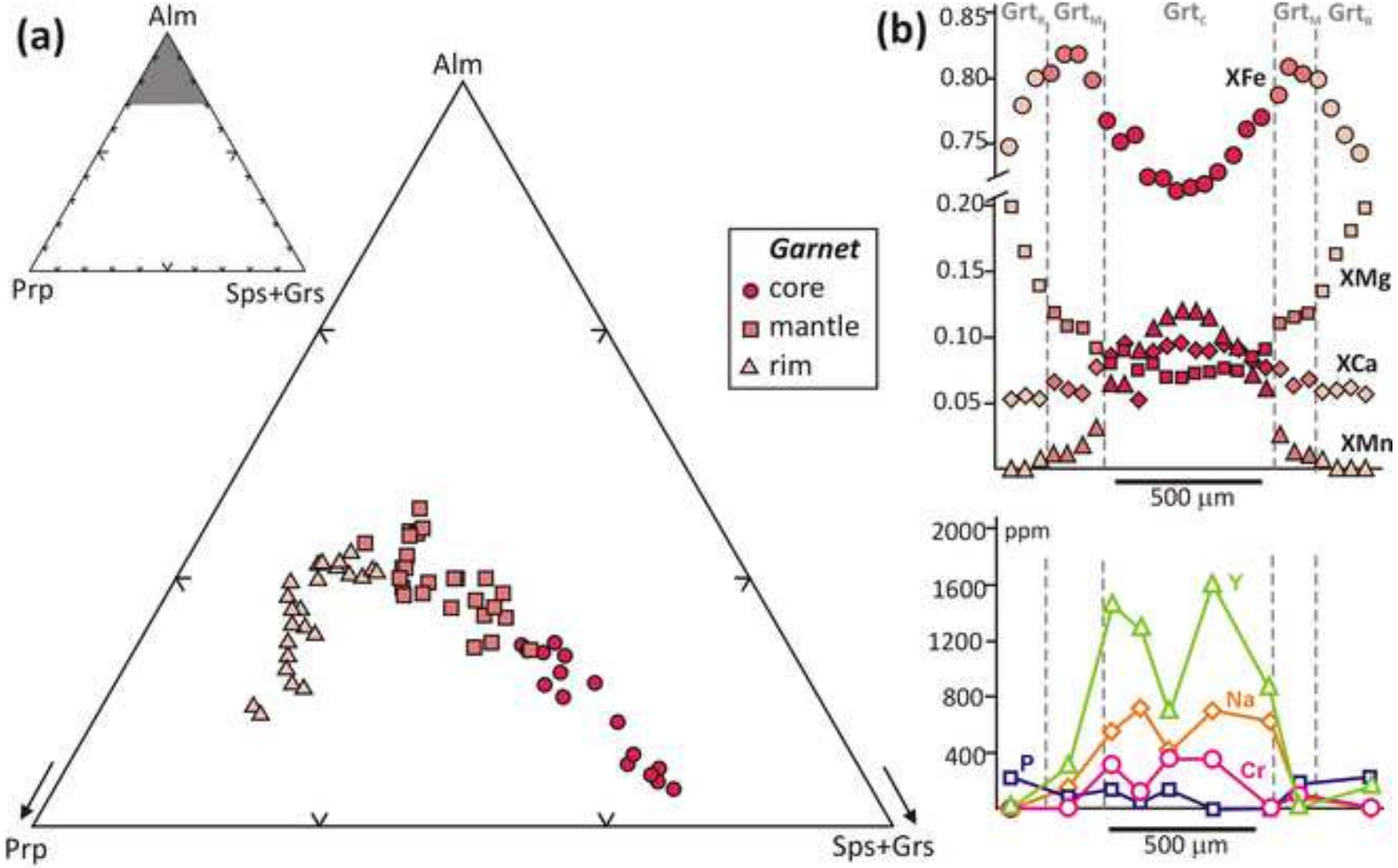

Fig. 6 **(a)** Garnet composition plotted in the Prp-Alm-(Sps+Grs) diagram (data from both samples US900 and US773). **(b)** Major and trace element chemical profile of a garnet porphyroblast from sample US900. Note the bell shaped profile of X_{Mn}, suggesting a prograde growth and the similar pattern of Y, Na and Cr.

Figure 7
Click here to download Figure: Fig7.tif

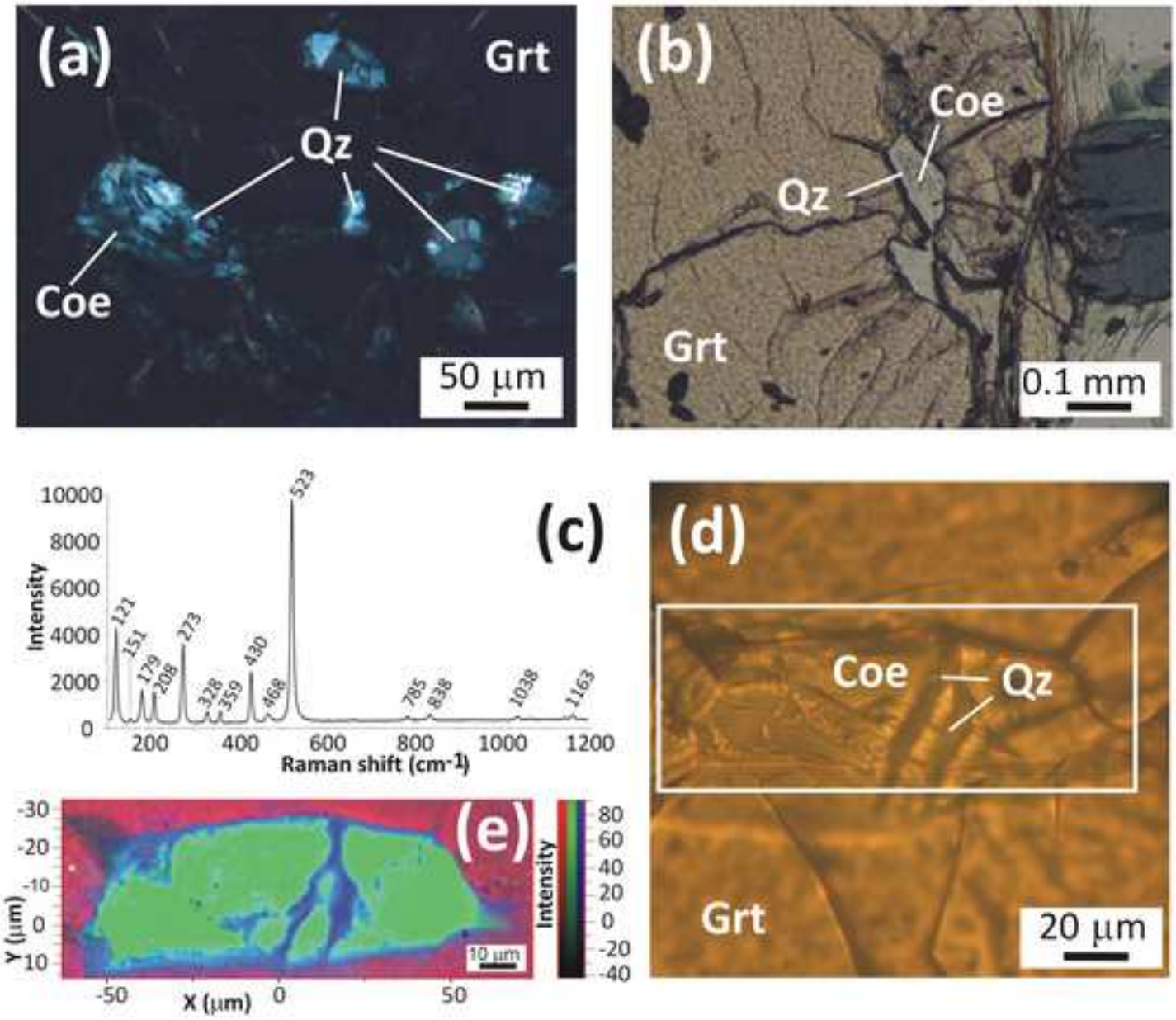

Fig. 7 **(a)** Microphotograph of large and relatively well preserved coesite inclusion within garnet mantle, and smaller polycrystalline quartz inclusions within garnet rim (US773; crossed polarized light). **(b)** Microphotograph of relatively small coesite inclusion, partly inverted to palisade quartz, within garnet rim (US773) (PPL). **(c)** Raman spectrum of coesite (US773). **(d)** Microphotograph of the mapped, well preserved coesite inclusion in garnet. The rectangle shows the mapped area reported in Fig. 7e (US773) (PPL). **(d)** Raman map of the spatial distribution and the intensity of the main peaks of coesite (524 cm^{-1}, in green), quartz (470 cm^{-1}, in blue), and garnet (917 cm^{-1}, in red). From the map is evident that the coesite inversion to quartz start from the grain-boundaries and the fractures.

Figure 8
Click here to download Figure: Fig8.tif

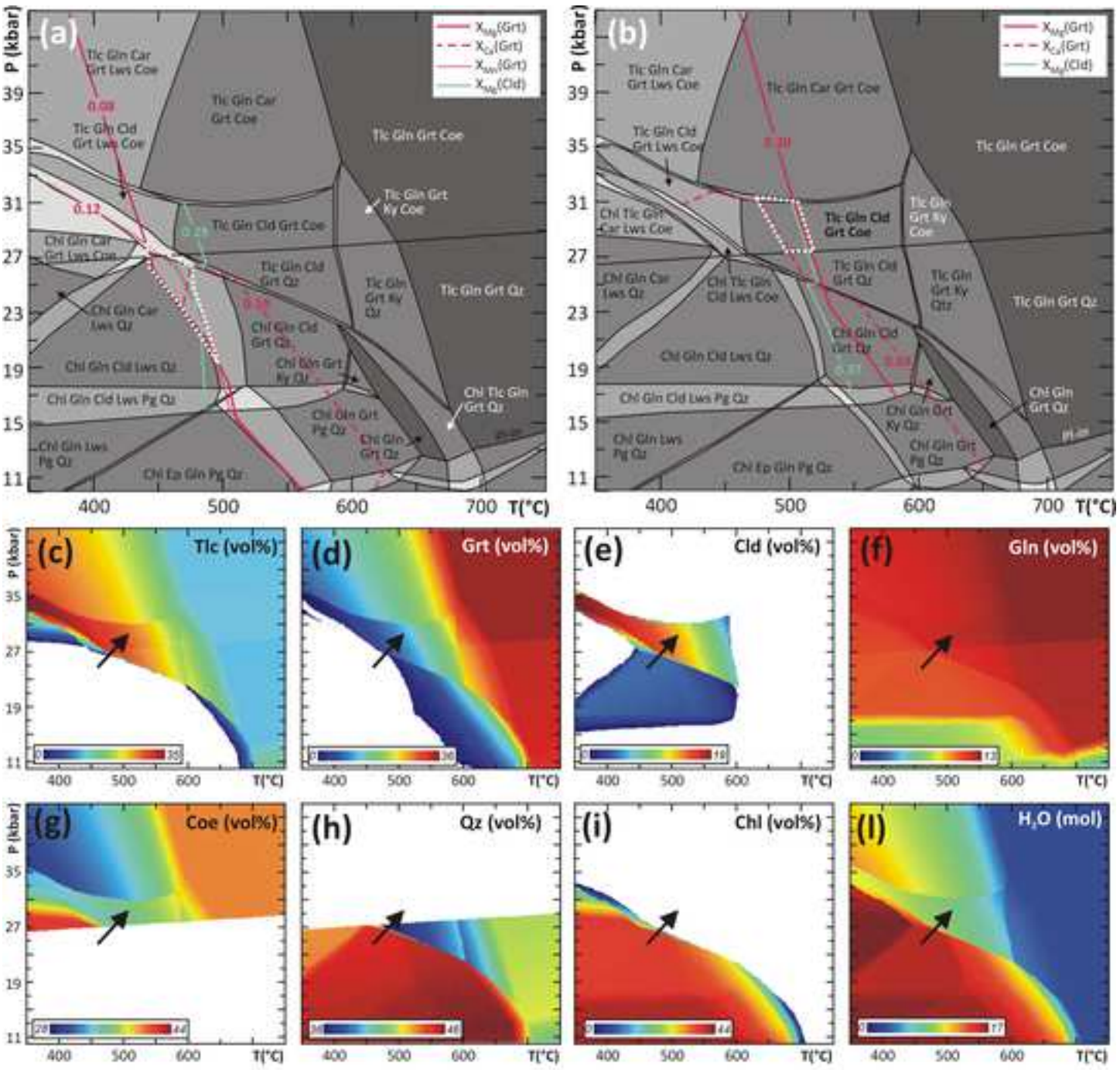

Fig. 8 **(a)** P-T pseudosection calculated for sample US900 in the MnNCFMASH system using the whole rock bulk composition (Table 3). The variance of the fields varies from three (i.e. 7 phases, light grey fields) to six (i.e. 4 phases, darker grey fields). Pink continuous, dashed and dotted lines are the X_{Mg}, X_{Ca} and X_{Mn} isopleths of garnet corresponding to the measured composition of garnet core; light blue continuous line is the X_{Mg} isopleth of chloritoid corresponding to the measured composition of chloritoid core. P-T conditions constrained for the growth of garnet core are represented by the white dotted polygon. **(b)** P-T pseudosection calculated for sample US900 using the fractionated bulk composition (whole rock composition minus garnet core and mantle; Table 3). The variance of the fields varies from three (i.e. 7 phases, light grey fields) to six (i.e. 4 phases, darker grey fields). Pink continuous, and dashed lines are the X_{Mg} and X_{Ca} isopleths of garnet corresponding to the measured composition of garnet rim; light blue continuous line is the X_{Mg} isopleth of chloritoid corresponding to the measured composition of chloritoid rim. P-T conditions constrained for the growth of garnet rim are represented by the white dotted polygon. **(c-l)** Modal variations (vol%) of the main mineral phases in sample US900 (c-i) and isomodes of water (mol) (l) calculated for the P-T pseudosection of Fig. 8b. Colours from blue to red imply higher modal proportions as indicated in each legend. The black arrow is the prograde P-T path constrained basing on the pseudosection results and YAG thermometry.

Figure 9
Click here to download Figure: Fig9.tif

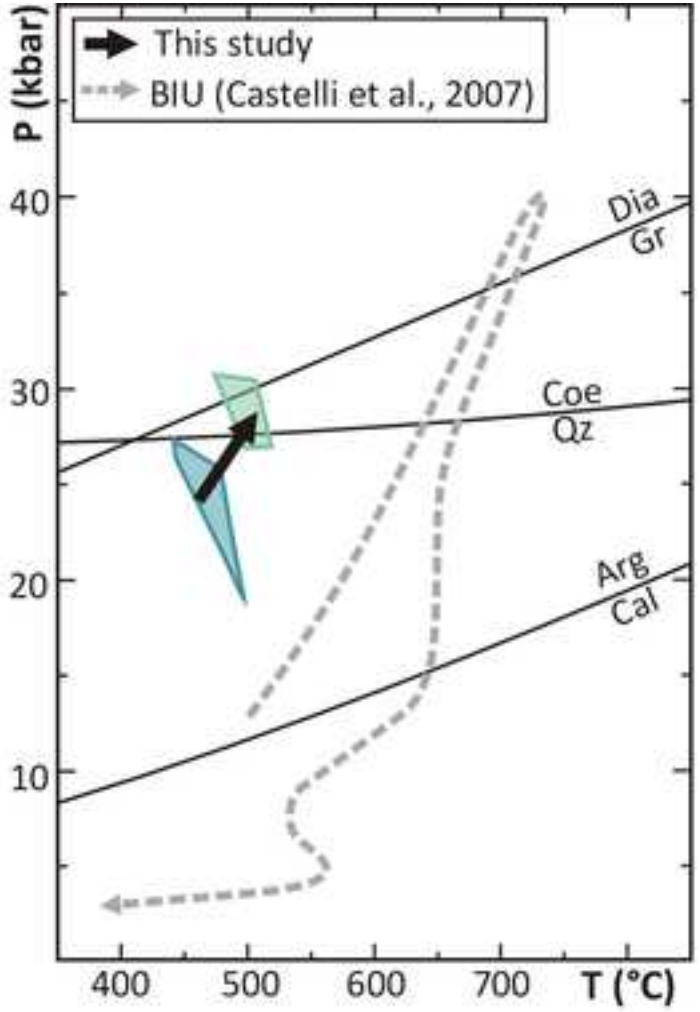

Fig. 9 Prograde P-T path (black arrow) inferred for the studied samples basing on the pseudosection results and YAG thermometry and comparison with the P-T evolution constrained for the adjacent UHP Brossasco-Isasca Unit (dashed grey arrow). The blue and light blue polygons represent the P-T conditions constrained for the growth of garnet core and rim, respectively (see Fig. 8a, b).

Table 1. Representative WDS a

Sample	US900									
Analysis	900_23 rim	900_24 mantle	900_25	900_26	900_27 core	900_28	900_29	900_30 mantle	900_31 rim	773_1 ri
SiO_2	37.52	36.86	37.40	37.01	36.60	36.88	37.14	36.89	37.32	37.67
P_2O_5	0.05	0.02	0.03	0.01	0.03	0.00	0.00	0.04	0.05	0.01
TiO_2	0.00	0.04	0.00	0.08	0.10	0.07	0.02	0.08	0.02	0.05
Al_2O_3	21.16	20.61	20.88	20.62	20.56	20.67	20.70	20.77	21.50	21.12
Cr_2O_3	0.00	0.00	0.05	0.02	0.05	0.05	0.00	0.01	0.00	0.00
Y_2O_3	0.00	0.04	0.18	0.16	0.08	0.20	0.11	0.00	0.02	0.00
FeO	34.93	37.01	35.15	33.06	32.19	33.34	34.55	36.73	34.33	35.23
MnO	0.16	0.54	1.80	4.01	4.77	4.34	2.80	0.47	0.16	0.18
MgO	4.40	2.77	2.34	1.96	1.79	1.93	2.18	2.89	4.72	4.48
NiO	0.00	0.03	0.02	0.00	0.24	0.00	0.00	0.00	0.11	0.00
CaO	1.90	2.01	2.70	2.79	3.10	2.80	2.60	2.17	2.00	1.70
Na_2O	0.00	0.02	0.07	0.10	0.06	0.09	0.09	0.01	0.00	0.00
K_2O	0.00	0.00	0.00	0.02	0.00	0.00	0.01	0.01	0.01	0.01
Total	100.10	99.95	100.62	99.83	99.56	100.36	100.19	100.06	100.22	100.44
Si	2.988	2.979	3.003	3.001	2.979	2.979	2.999	2.974	2.960	2.992
P	0.003	0.001	0.002	0.001	0.002	0.000	0.000	0.003	0.003	0.001
Ti	0.000	0.002	0.000	0.005	0.006	0.004	0.001	0.005	0.001	0.003
Al	1.986	1.964	1.976	1.971	1.972	1.967	1.969	1.973	2.010	1.977
Cr	0.000	0.000	0.003	0.001	0.003	0.003	0.000	0.001	0.000	0.000
Y	0.000	0.002	0.008	0.007	0.004	0.009	0.005	0.000	0.001	0.000
Fe^{+3}	0.033	0.073	0.015	0.025	0.056	0.069	0.041	0.069	0.063	0.034
Fe^{+2}	2.293	2.429	2.345	2.217	2.135	2.183	2.292	2.407	2.214	2.306
Mn	0.010	0.037	0.123	0.275	0.329	0.297	0.192	0.032	0.011	0.012
Mg	0.522	0.334	0.281	0.237	0.217	0.233	0.262	0.348	0.558	0.531
Ni	0.000	0.002	0.001	0.000	0.016	0.000	0.000	0.000	0.007	0.000
Ca	0.162	0.174	0.232	0.242	0.270	0.243	0.225	0.187	0.170	0.144
Na	0.000	0.003	0.011	0.015	0.009	0.014	0.014	0.002	0.000	0.000
K	0.000	0.000	0.000	0.002	0.000	0.000	0.001	0.001	0.001	0.001
XMg	0.18	0.11	0.09	0.08	0.08	0.08	0.09	0.12	0.19	0.18
XFe	0.77	0.82	0.78	0.74	0.72	0.74	0.77	0.81	0.75	0.77
XCa	0.05	0.06	0.08	0.08	0.09	0.08	0.08	0.06	0.06	0.05
XMn	0.00	0.01	0.04	0.09	0.11	0.10	0.06	0.01	0.00	0.00

Structural formulae have been calculated on the basis of 12 oxygens. Fe^{+3} has been calculated by stoichiometry.

nalysis of garnet

				US773					
773_2	773_3	773_4	773_5	773_6	773_7	773_8	773_9	773_10	773_11
m		mantle		core	mantle			rim	
36.99	36.84	36.93	37.21	36.82	36.85	36.91	37.19	37.18	37.68
0.05	0.09	0.01	0.05	0.00	0.04	0.00	0.00	0.12	0.00
0.07	0.07	0.11	0.05	0.07	0.05	0.17	0.06	0.01	0.15
20.67	20.63	20.19	20.40	20.34	20.72	20.49	20.73	20.96	21.28
0.00	0.05	0.04	0.04	0.05	0.01	0.07	0.00	0.00	0.00
0.00	0.12	0.02	0.00	0.25	0.00	0.02	0.00	0.00	0.00
36.50	36.96	36.80	35.86	34.39	35.78	35.86	36.47	35.91	34.84
0.16	0.32	0.58	1.23	2.72	1.15	0.37	0.19	0.11	0.12
3.72	2.82	2.41	2.29	2.22	2.52	2.94	3.33	4.00	4.62
0.00	0.00	0.14	0.00	0.05	0.09	0.17	0.13	0.14	0.00
1.50	2.54	2.87	3.01	3.12	2.89	2.62	2.08	1.48	1.84
0.00	0.03	0.02	0.00	0.07	0.03	0.00	0.04	0.03	0.01
0.00	0.00	0.00	0.01	0.00	0.02	0.00	0.02	0.02	0.01
99.64	100.47	100.12	100.15	100.09	100.15	99.63	100.23	99.95	100.55
2.981	2.959	2.986	3.004	2.979	2.970	2.986	2.983	2.977	2.984
0.003	0.006	0.000	0.003	0.000	0.003	0.000	0.000	0.008	0.000
0.004	0.004	0.007	0.003	0.004	0.003	0.011	0.004	0.001	0.009
1.963	1.953	1.924	1.942	1.939	1.967	1.954	1.960	1.978	1.986
0.000	0.003	0.003	0.003	0.003	0.001	0.004	0.000	0.000	0.000
0.000	0.005	0.001	0.000	0.011	0.000	0.001	0.000	0.000	0.000
0.062	0.108	0.090	0.037	0.091	0.089	0.048	0.075	0.061	0.030
2.398	2.375	2.398	2.384	2.235	2.323	2.378	2.372	2.343	2.278
0.011	0.022	0.040	0.084	0.186	0.078	0.025	0.013	0.007	0.008
0.447	0.338	0.291	0.276	0.267	0.303	0.355	0.399	0.477	0.546
0.000	0.000	0.009	0.000	0.003	0.006	0.011	0.008	0.009	0.000
0.130	0.219	0.249	0.260	0.270	0.250	0.227	0.179	0.127	0.156
0.000	0.005	0.003	0.000	0.011	0.005	0.000	0.006	0.005	0.002
0.000	0.000	0.000	0.001	0.000	0.002	0.000	0.002	0.002	0.001
0.15	0.11	0.10	0.09	0.09	0.10	0.12	0.14	0.16	0.18
0.80	0.80	0.80	0.79	0.75	0.78	0.79	0.80	0.79	0.76
0.04	0.07	0.08	0.09	0.09	0.08	0.08	0.06	0.04	0.05
0.00	0.01	0.01	0.03	0.06	0.03	0.01	0.00	0.00	0.00

Table 2

Table 2. Representative SEM-EDS analysis of chloritoid, g

Chloritoid						Amphibole			
Sample	US900		US773			Sample	US900		
Analysis	2Ctd2 core	2Ctd3 rim	1Ctd46 in Grt	2Ctd11 core	2Ctd12 rim	Analysis	2Gln8 core	2Gln9 rim	1Gln60 core
SiO_2	24.79	24.87	24.20	24.51	24.75	SiO_2	56.30	56.22	56.25
Al_2O_3	38.80	38.57	37.78	37.57	37.70	Al_2O_3	8.24	9.46	7.60
FeO	22.97	22.17	26.81	24.70	23.35	FeO	12.38	8.91	13.09
MnO	0.00	0.00	0.00	0.00	0.00	MnO	0.00	0.00	0.00
MgO	5.47	6.25	3.54	4.84	5.89	MgO	10.27	11.04	10.32
CaO	0.00	0.00	0.00	0.00	0.00	CaO	0.00	0.00	0.00
Na_2O	0.00	0.00	0.00	0.00	0.00	Na_2O	6.58	6.70	6.53
K_2O	0.00	0.00	0.00	0.00	0.00	K_2O	0.00	0.00	0.00
Total	92.03	91.86	92.33	91.61	91.68	Total	95.87	94.42	95.89
Si	2.027	2.026	2.008	2.029	2.031	Si	8.035	8.051	8.043
Al	3.737	3.704	3.694	3.664	3.646	Al	1.386	1.597	1.281
Fe^{+3}	0.210	0.244	0.290	0.278	0.292	Fe^{+3}	0.555	0.299	0.646
Fe^{+2}	1.360	1.267	1.570	1.432	1.311	Fe^{+2}	0.922	0.768	0.920
Mn	0.000	0.000	0.000	0.000	0.000	Mn	0.000	0.000	0.00
Mg	0.666	0.759	0.438	0.597	0.720	Mg	2.185	2.357	2.200
Ca	0.000	0.000	0.000	0.000	0.000	Ca	0.000	0.000	0.000
Na	0.000	0.000	0.000	0.000	0.000	Na	1.821	1.860	1.810
K	0.000	0.000	0.000	0.000	0.000	K	0.000	0.000	0.000
XMg	0.33	0.38	0.22	0.29	0.36	XMg	0.70	0.75	0.71
XFe^{+3}	0.05	0.06	0.07	0.07	0.07	XFe^{+3}	0.29	0.16	0.34

Structural formulae have been calculated on the basis of 14 oxygens for chloritoid, 13CNK (Si+Al+Mg+Ti+Mn+Fe=13) fc

Fe^{+3} has been calculated by stoichiometry except for amphibole (average Fe^{+3} values).

laucophane, talc and Mg-chlorite

			Talc			Chlorite
US773		Sample	US900	US773		US773
1Gln62 rim	1Gln70 o-rim	Analysis	1Tlc27	2Tlc23		2Chl21
56.97	54.71	SiO_2	61.53	61.49	SiO_2	27.95
9.43	4.32	Al_2O_3	0.00	0.00	Al_2O_3	20.06
9.39	10.76	FeO	6.94	6.99	FeO	17.31
0.00	0.00	MnO	0.00	0.00	MnO	0.00
11.08	15.56	MgO	26.50	26.19	MgO	22.05
0.00	3.01	CaO	0.00	0.00	CaO	0.00
6.68	2.87	Na_2O	0.00	0.00	Na_2O	0.00
0.00	0.00	K_2O	0.00	0.00	K_2O	0.00
95.67	93.30	Total	94.97	94.67	Total	87.36
8.064	7.937	Si	4.032	4.046	Si	2.825
1.573	0.739	Al	0.000	0.000	Al	2.390
0.291	0.953	Fe^{+3}	0.000	0.000	Fe^{+3}	0.000
0.821	0.352	Fe^{+2}	0.380	0.385	Fe^{+2}	1.463
0.00	0.00	Mn	0.000	0.000	Mn	0.000
2.338	3.365	Mg	2.588	2.569	Mg	3.322
0.000	0.468	Ca	0.000	0.000	Ca	0.000
1.833	0.807	Na	0.000	0.000	Na	0.000
0.000	0.000	K	0.000	0.000	K	0.000
0.74	0.91	XMg	0.87	0.87	XMg	0.69
0.16	0.56					

or amphibole, 12 oxygens for talc and 18 oxygens for chlorite.

Table 3. Bulk compositions (wt%) and modal amounts (vol%) of the main mineral phases

Sample	US900	US900*	US773
SiO_2	66.45	67.01	51.56
Al_2O_3	10.49	10.3	18.52
MgO	10.67	10.84	13.37
CaO	0.21	0.17	0.19
MnO	0.08	0.01	0.06
FeO	10.13	9.65	14.92
Fe_2O_3	1.05	1.08	1.09
Na_2O	0.93	0.95	0.29
Total	100.0	100.0	100.0
Qz/Coe	38.4		21.4
Tlc	30.5		22.3
Cld	14.0		22.6
Grt	7.9		8.1
Gln	9.2		2.8
Mg-Chl	<1		22.8

* effetive bulk composition in equilibrium during the growth of Grt rim (whole rock composition minus the garnet core and mantle compositions)

Supplementary data
Click here to download Supplementary data: Supplementary material.pdf

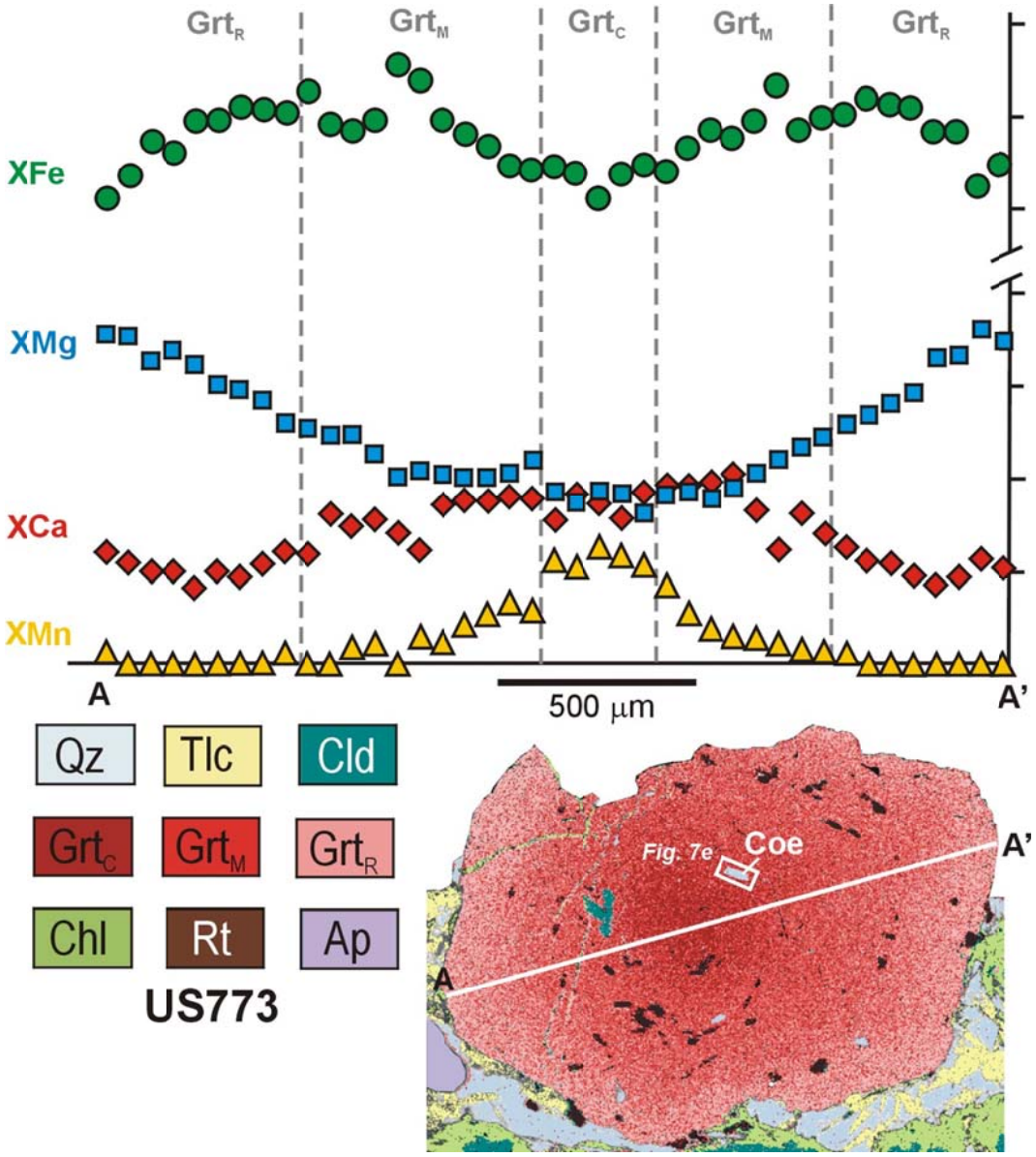

Fig. S1 - Major element chemical profile and processed X-ray map of a garnet porphyroblast from sample US773.

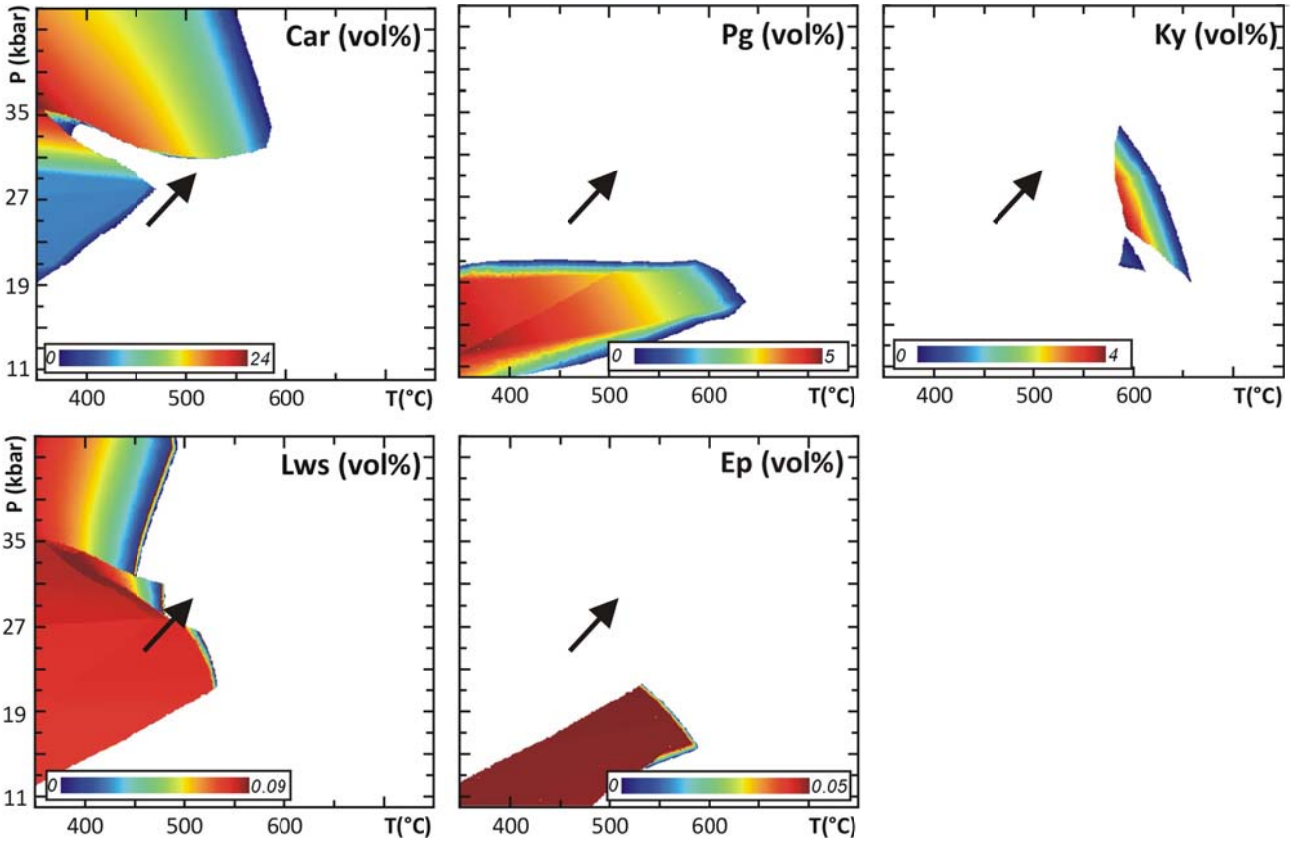

Fig. S2 - Modal variations (vol%) of mineral phases in sample US900, not reported in Fig. 8. Colours from blue to red imply higher modal proportions as indicated in each legend. The black arrow is the prograde P-T path constrained basing on the pseudosection results and YAG thermometry.

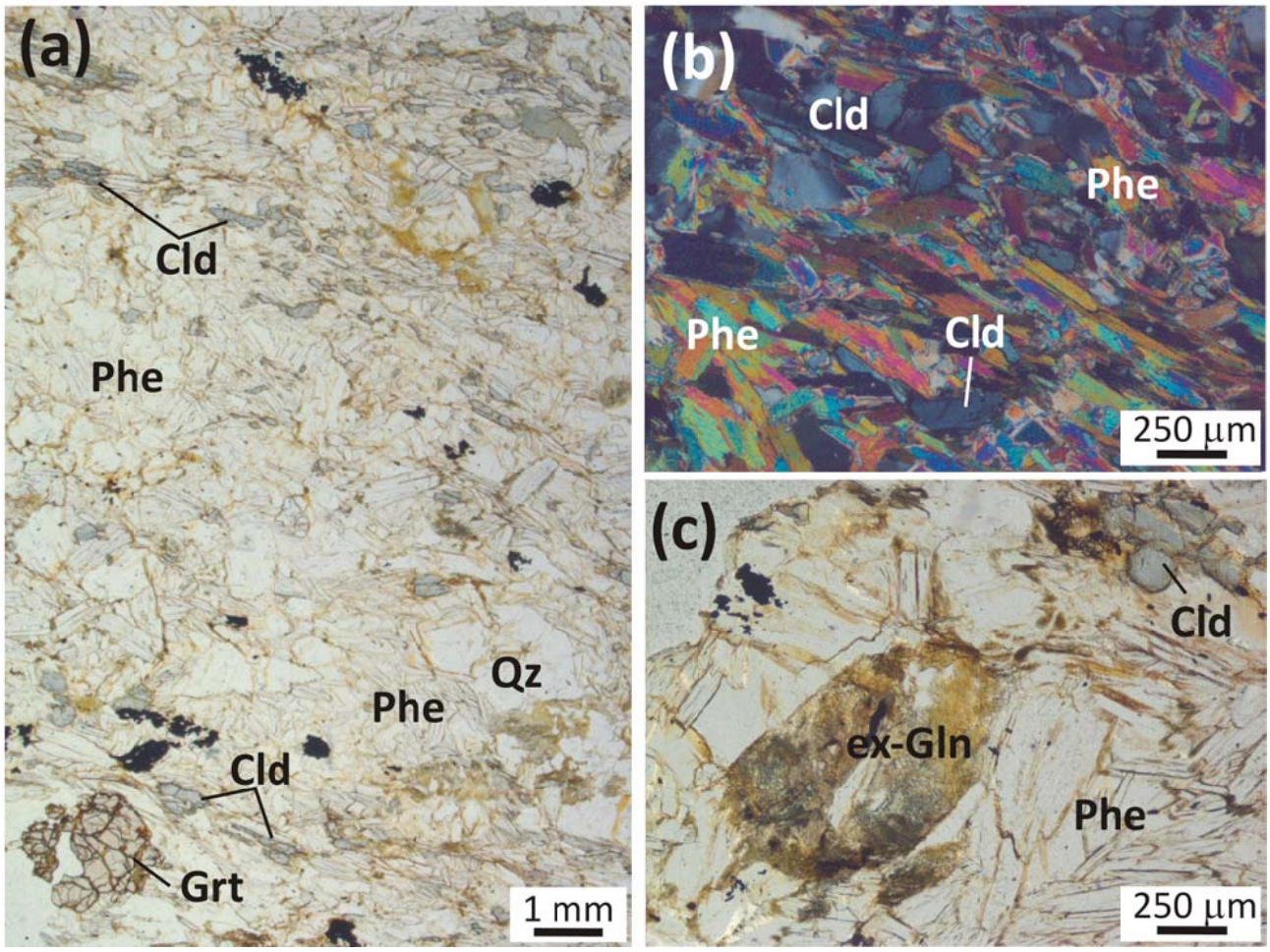

Fig. S3 - Sample LA13. (a) Representative microstructure of sample LA13 (PPL). (b) Detail of the main foliation defined by Phe and Cld (XPL). (c) Wm + Bt + Chl pseudomorph after former Gln (PPL).